Single-cell Transcriptomics Unravel Stereocilia Degeneration as a Key Contributor to Age-related Vestibular Dysfunction in Mice and Humans

Samadhi Kulasooriya[1*], Huizhan Liu[1], Sarath Vijayakumar[1], Celia Bloom[1], Su Tu[1], Benjamin J. Borgmeier[1], Mi Zhou[1], Litao Tao[1], Bechara Kachar[2], David Z. He[1*]

[1]Department of Biomedical Science, School of Medicine, Creighton University, Omaha, Nebraska, USA

[2]Laboratory of Cell Structure and Dynamics, National Institute of Deafness and Other Communication Disorders, National Institutes of Health, Bethesda, Maryland, USA

Corresponding authors:

David Z. He (DavidHe@creighton.edu)

Samadhi Kulasooriya (SamadhiKulasooriya@creighton.edu)

Abstract

Age-related vestibular dysfunction (ARVD) is a prevalent, debilitating condition in the elderly. The etiology and molecular mechanisms are poorly understood. We focused on mechanosensitive hair cells (HCs) as they are particularly vulnerable to aging. Using single-cell RNA-seq transcriptomes of young and old mouse vestibular HCs, we show that aging HCs display both universal molecular blueprints, such as genomic instability, mitochondrial dysfunction, and impaired proteostasis, and cell type-specific aging signatures associated with deterioration of hair bundles and mechanotransduction. These signatures are also observed in aged human vestibular HCs, suggesting shared mechanisms. Importantly, morphological and functional analysis revealed that bundle degeneration and vestibular functional decline precede HC loss, highlighting the deterioration of mechanotransduction as a key contributor to ARVD. Furthermore, molecular and cellular changes associated with aging signatures are less pronounced in vestibular HCs than in cochlear HCs, underscoring the different pace of aging between the two mammalian inner ear sensory epithelia.

Introduction

Aging research has experienced unprecedented advances in recent years, revealing that genetic and molecular processes conserved through evolution may partially govern the pace of aging[1]. Aging is the progressive deterioration of physiological integrity, leading to impaired function, and enhanced vulnerability to disease and death. The molecular processes of aging are characterized by the universal hallmarks of aging including increased cellular senescence, genomic instability, epigenetic alterations, mitochondrial dysfunction, loss of proteostasis, and inflammaging. The interconnected and interdependent nature of these processes leads to slow age-related structural changes and functional decline[1,2]. Similar to other sensory organs, biological aging negatively impacts the inner ear, resulting in age-related hearing loss (ARHL) and vestibular dysfunction (ARVD). While numerous studies have focused on ARHL, ARVD remains relatively understudied partially due to its multifaceted etiology[3–8]. ARVD is characterized by the gradual loss of bilateral vestibular function accompanied by interruptions to visual and proprioceptive inputs. The damaging impact of age-related vestibular sensory decline manifests itself in an exponential increase in geriatric dizziness and injurious/fatal falls[9]. According to the National Center for Health Statistics and National Institutes of Health, the prevalence of ARVD in the US is 75.3%. It is the 6th leading cause of death and accounts for 50% of all accidental deaths among the elderly population[6,10]. Despite the high prevalence, currently, there are no targeted treatments to prevent or mitigate ARVD[11].

While the central neural pathways in the vestibular system play a role in ARVD, age-related degeneration of vestibular neurons and HCs in the vestibular periphery contribute to ARVD[11]. The vestibular system plays a crucial role in sensing the direction, acceleration, and spatial orientation of the head in response to gravity to maintain the upright posture and balance of the body. It consists of three crista ampullaris that detect the angular motions and two otolith organs (utricle and saccule) that detect linear motions of the head[12]. Vestibular sensory epithelia consist of two types of mechanosensitive hair cells (HCs), type I and type II HCs. HCs convert mechanical stimuli into electrical signals. Mechanotransduction, the first step in the vestibular signal processing, is mediated by the mechanotransduction apparatus in the hair bundle comprising tightly linked stereocilia and a kinocilium[13,14]. Therefore, damage or deterioration of hair bundles will lead to vestibular functional decline[11,13–16]. Interestingly, studies from human and murine models indicate an earlier and more pronounced auditory functional and morphological decline compared to the vestibular system, highlighting tissue-specific differences between these sensory organs[8,9]. However, molecular mechanisms driving these divergent aging processes remain unknown. This fundamental lack of understanding of the molecular basis of vestibular aging remains a significant barrier to developing targeted therapeutic interventions to mitigate ARVD[17].

While previous studies have examined age-related physiological and morphological changes in the vestibular system, no studies have been performed to characterize universal and cell type-specific signatures of aging in vestibular HCs. In the current study, we comprehensively examined the aging of the vestibular system across functional, morphological, and molecular levels. Transcriptomic studies have been at the forefront of revealing the molecular underpinnings of development, aging, and disease conditions in model organisms and humans. Utilizing single-cell RNA sequencing (scRNA-seq), we characterized universal and cell-type aging signatures in vestibular HCs from young and aged mice, with findings corroborated by human datasets. The unique aging signatures are primarily associated with the deterioration of hair bundles and mechanotransduction apparatus. Concordant with that, electrophysiology and imaging revealed that vestibular functional decline and bundle degeneration precede HC loss, highlighting the deterioration of the stereocilia bundle as a key contributor to ARVD. Additionally, we observed tau accumulation in aging vestibular HCs similar to what has been observed in neurons of neurodegenerative diseases. The comparison between vestibular and cochlear HCs shows that the age-related molecular and cellular changes are less pronounced in vestibular HCs than in cochlear HCs, underscoring the subtle differences in aging between the two sensory epithelia in the mammalian inner ear. Our data provide a foundational transcriptomic resource to advance the understanding of inner ear aging and the development of targeted therapeutic strategies.

Results

Age-related functional and morphological alterations in the vestibular HCs

Prior studies have reported various age-related functional and structural changes in the vestibular system[6,7,18,19]. In this study, we utilized CBA/J mice, which exhibit progressive age-related changes in the inner ear function resembling that of humans[20,21](Fig. 1). To examine the age-related functional decline in the vestibular system, we measured vestibular sensory evoked potentials (VsEP) from young and old animal cohorts. This test measures electrical signals in response to rapid linear accelerations by evaluating sensitivity (threshold), strength of the response (amplitude), and time taken by the signal to reach the recording electrode after stimulus initiation (latency)[22,23]. Consistent with previous findings, our results indicated an age-related decline in the vestibular function, as evidenced by a significant decrease in the response amplitude and an increase in the threshold and latency (Fig.1A-C). We also measured endolymphatic potential (ELP), which is crucial to maintain the ionic gradient required for mechanotransduction[24], and it typically ranges from +1 to +11mV[25–27]. Our findings revealed no age-related change in ELP, indicating maintenance of a stable electrochemical environment (Fig.1D).

Next, we examined the age-related morphological alterations in vestibular HCs. Previous studies have reported an age-related loss of vestibular HCs in both mice and humans[7,28,29], with type I HC loss being higher than type II HCs[6], while some studies indicate no HC loss[30]. Thus, to re-examine the age-related HC loss, we immunolabeled young and old utricles with HC-specific marker MYO7A and distinguished between type I and II vestibular HCs via SOX2 expression, which is seen in type II HCs only[31–33]. Our findings showed no age-related changes in type I and II HC density in the striolar and extrastriolar regions (Fig.1E, F). Cellular hypertrophy and atrophy are commonly seen in aging cells, including cochlear HCs and neurons[34,35]. To further assess the age-related vestibular cytological alterations, we conducted a histological analysis (Fig.1G). While we noted cellular hypertrophy and atrophy in some cells in the vestibular end organs, there were no significant alterations in the overall integrity (Fig.1H, I). Next, we utilized imaging techniques to examine the age-related changes in the hair bundle (Fig.1J, K). We noted signs of stereociliopathy, including loss, and fusion of stereocilia, alongside degeneration of kinocilia. Collectively, these findings indicate various age-related cytological alterations, particularly in the hair bundle that may impair sensory mechanotransduction, leading to vestibular functional decline indicated by VsEP, contributing to ARVD.

Cellular diversity in young and old vestibular end organs

The molecular mechanisms underlying age-related vestibular degeneration are poorly understood[17]. To unveil this, we conducted single-cell RNA-sequencing of inner ears harvested from 10-week- and 22-month-old CBA/J mice. The sequencing reads were aligned to the mouse reference genome (mm10), followed by standard quality control metrics and downstream processing steps, including dimensional reduction and unsupervised clustering[36](Fig.2A, Supplementary Fig.1). Cell clusters were annotated based on known marker gene expression and gene signatures (Fig.2B, C). We observed that the cellular diversity is largely preserved between young and old samples, encompassing type I and II HCs, SCs, and blood, neuronal, immune, and epithelial cell populations. We annotated with their top marker genes for certain clusters in both cohorts where definitive identities could not be assigned. HCs were identified based on the expression of markers such as *Myo6, Otof, Slc17a8, Pou4f3*[37–39], and type I and II HC types were differentiated using Sox2[31,32](Fig.2D, E, G, H). Based on these markers, 698 (type I) and 129 (type II) from young samples and 1651 (type I) and 230 (type II) from old samples were isolated for the downstream analysis (Fig.2F, I). Additionally, we noted the presence of nine transcriptionally distinct subclusters within both young and old primary HC clusters, originating from the three vestibular end organs, reflecting their intra-HC distribution and regional differences. Based on the known markers, we pinpointed the regional origins of these populations within the vestibular system (Supplementary Fig.2, 3).

Universal hallmarks of aging

Cellular aging typically follows universal aging programs[1,2]. Prior studies have demonstrated that cochlear HC aging is associated with universal hallmarks such as mitochondrial dysfunction, oxidative stress, and apoptosis[17]. Thus, we speculated that aging vestibular HCs may also exhibit universal hallmarks. We aggregated single-cell data to generate pseudobulk expression matrices, and these counts were analyzed using genes identified from multiple resources as described in methods (Fig.4A). Cellular senescence is characterized by the permanent cessation of the cell cycle. Senescent cells adopt the characteristic senescence-associated secretory phenotypes (SASP), which exerts deleterious effects on cellular function over time and is recognized as a hallmark of cellular aging[40]. Our data indicated a decrease in cell cycle regulators (*Cdk2, Cdk4, Cdk6*), followed by an increase in cyclin-dependent kinase inhibitors (*Cdkn1a, Cdkn1b*), and degradation of cyclins (*Fzr1*) indicating cell cycle arrest. Moreover, we noted an increase in senescence induction (*Ypel3*), a decrease in laminins (*Lmna, Lmnb1*), and enrichment of various SASPs that are involved in inflammation (*Cxcl14, Nfkb2, B2m*), senescence-associated heterochromatic foci (*H3f3a, Hira, Ubn1*), hypoxia and angiogenesis (*Vegfa, Hif1a, Nos3*) indicating increased senescence in old HCs relative to young HCs. The imbalance between the production and elimination of reactive oxygen species (ROS) results in oxidative stress[1,2]. We observed an increased expression of genes involved in mitochondrial respiration, the major contributor of ROS generation (*Cox4i1, Cox6a1, mt-Co1, mt-Cytb, Ndufs2*), antioxidant response and detoxification (*Mt1, Sod1, Prdx1, Gpx4, Keap1, Nrf1*), mitochondrial fission and fusion (*Fis1, Mfn1, Mfn2*), stress response (*Bcl2, Atf4, Cflar, Hif1a, Atf4, Atf5*) and mitochondrial quality control (*Lonp1, Trap1*), suggesting age-related increase in oxidative stress followed by a compensatory increase in antioxidant mechanisms. In addition, we noticed a decrease in key genes involved in the detoxification of hydrogen peroxide, such as *Gpx1, Prdx1, Sod3*, and *Cat*, indicating partial ROS clearance. Age-related gradual increase in chronic low-grade inflammation is termed inflammaging[1,2]. We noticed a steady increase in pro-inflammatory genes (*Ptgds, Cxcl14, Ccl12, Il1a, Nfkb1, Jak1, Stat3, Tradd, Fadd, Irak1, Mapk1, Mapk14*) and downregulation of some genes (*Tgfb1, Cxcl12, Tlr3, Tlr4, Myd88, Irak4, Ccl2, Ccl5, Ccl11*), indicating potential maintenance of a prolonged low-grade inflammatory state followed by reduced immune surveillance and response. Epigenetic dysregulation increases with aging[41]. Our data demonstrated age-related epigenetic alterations, including the reduction in global heterochromatin (*Kdm5a, Kdm6a, Ezh1, Ezh2, Setdb2, Smarcb1*), nucleosome remodeling (*Smarca1, Ino80b, Vps72, Phf8, Chd4, Chd5, Anp32e, Itgb3bp, Ssrp1, Baz2a*), changes in histone marks (*Mll1, Mll3, Setd2, Kdm4a, Hdac3, Hdac4, Ctcf, Cbx3*), global DNA hypomethylation, and CpG hypermethylation (*Dnmt1, Dnmt3b, Tet1, Ezh1, Ezh2*). Age-driven dysregulation of mechanisms involved in protein synthesis, folding, and turnover leads to impaired protein homeostasis, followed by the accumulation of misfolded protein aggregates. We noted the downregulation of genes involved in misfolded/unfolded protein response (*Hspb1, Hspb2, Dnajb5, Dnajb14, Dnajc24, Dnajc5, Vcpip*) and protein turnover (*Ube2e2, Usp38, Uch15, Rnf38, Fbxo31, Fbxw8*) indicating signs of impaired proteostasis. Reduced DNA repair capability accumulates DNA damage leading to genome instability with aging[1,2]. We observed a decrease in the expression of the genes involved in DNA damage response (*Trp53, Mdm2, Chek1, and Chek2*) and repair mechanisms (*Rad50, Rad52, Xpc, Xrcc1, Xrcc2, Atr, Atm, Mgmt, Apex1, Recql*) indicating diminished DNA repair in old vestibular HCs. Autophagy is crucial to recycle damaged organelles to maintain cellular homeostasis[1,2]. We noted the enrichment of key genes related to autophagy initiation, autophagosome formation, and progression (*Becn1, Atg12, Atg13, Atg16l1, Atg101, Map1lc3b, Ulk1, Ulk2, Fundc1, Tbk1, Pink1, Sqstm1, Tsc2, Bnip3*). However, we also noticed the downregulation of key genes (*Atg5, Atg7, Atg9a, Atg9b, Atg10, Atg14, Prkaa1, Prkaa2, Ambra1, Nrbf2, Lepr, Ppargc1a*) that involves in autophagosome elongation, autophagy progression, and energy sensing. While this may suggest active regulation of autophagy, there are signs of dysregulation in autophagosome formation and energy sensing. Aging impacts the extracellular matrix (ECM) dynamics and intercellular communication[1,2]. Our data indicated a reduction in genes involved in cell-cell adhesion (*Cdh1, Cdh3, Cdh15, Pcdh17, Pcdh9, Pcdhga4, Ptprk, Ptprf*), intercellular communication (*Gja1, Gjb2, Nlgn1, Nlgn2*), ECM interactions and diminished tissue integrity (*Itgb1,*

Itgav, Itga8, Tjp3, Cldn10, Cldn23). We used RNAscope *in situ hy*bridization to validate some key markers identified from our analysis (Fig. 3B). Previous studies show that the downregulation of proteostasis regulator, *Hspb1* (encodes for Heat-shock protein 27) is associated with ARHL[42]. Moreover, gap-junction marker *Gjb2* (encodes for connexin 26) is associated with genetic deafness accompanied by vestibular dysfunction[43]. *Mt1* (encodes for metallothionine1) plays a dual role in oxidative stress response and inflammation. While it plays a protective role in response to high oxidative stress, it negatively regulates immune response by impairing the STAT signaling pathway and is associated with autoimmune and inflammatory diseases[44]. We validated the decrease in *Hspb1, Gjb2,* and increase in *Mt1* expression with biological aging, which may play roles in ARVD. Together, these data indicate that vestibular HC aging is associated with universal aging programs.

Cell-type specific aging signatures

Previous studies have revealed distinct cell-type-specific aging signatures across various tissues[45]. Hence, we examined whether the universal vestibular HC aging programs are accompanied by cell-type specific aging signatures (Fig.4). We performed PCA multivariate analysis to examine the overall age-driven changes in the gene expression in young and old type I and II HCs across our 5 biological replicates. Our results show that the most striking differences in our datasets occur between young and old groups, rather than between type I and II HC subtypes, as evidenced by the 96% variance of principal component 1 (Fig.4A). Next, we assessed the number of unique and shared genes expressed in young and old type I and II HCs. We noted that irrespective of cell type or age, the majority of genes (60.7%) are shared among HCs. However, we observed an increase in the number of unique genes expressed in type I with age, accompanied by a reduction in the number of unique genes expressed in type II, indicating subtle age-driven transcriptomic changes between the two HC types (Fig.4B). To evaluate these differences between old HCs compared to young HCs, we conducted a differentially expressed gene (DEG) analysis (Fig.4C, D). Although many DEGs were identified, we primarily focused on the genes associated with universal or cell-type-specific aging signatures (Fig.4E). Our DEG analysis revealed age-related downregulation of hair bundle-related genes, including *Ush1c, Espn, Cib2, Dynll2, Tubb4b, Actb, Gsn, Calm1, Calm2, Tekt1, Tekt2, Nudc, Evl, Cfap46,* and *Atp2b2*, most of which are associated with genetic balance disorders and hearing loss[46–51]. Downregulation of these genes in the vestibular HCs during biological aging may play a crucial role in the development of ARVD and could serve as potential biomarkers. Additionally, many of our top enriched DEGs are linked to universal hallmarks, including oxidative stress (*mt-Co1, mt-Atp6, Mt1*), inflammation (*Ptgds*), and epigenetic alterations (*Pifo, Tle5, Chrac1, Gtf2i*) while top downregulated DEGs were associated with proteostasis (*Hsbp1, Hsp90ab1, Cct7, Erp29, Fbxo2, Uba52*), and intercellular communication (*Dctn3, Epcam, Afdn*). Previous studies have suggested that type I HCs are more vulnerable to aging than type II[9]. While we did not observe significant intercellular aging differences at the cellular and molecular levels, we observed heterogeneity in gene expression among individual HCs (Supplementary Fig.4). Overall, these findings suggest that vestibular HCs exhibit both cell-type-specific and universal aging signatures, which may play roles in ARVD.

Biological processes downregulated in old vestibular HCs

To examine the biological relevance of our observed DEGs, we performed gene ontology (GO) enrichment analysis and Kyoto Encyclopedia of Genes and Genomes (KEGG) analysis (Fig.5). We observed a notable downregulation of GO terms related to i) HC structure and functions including cilia motility, organization, and cytoskeleton, ii) proteostasis-related processes such as regulation of protein ubiquitination, proper protein folding, and refolding, iii) synapsis, iv) sensory perception of mechanical stimuli indicating the age-driven decline of several key functional processes in old HCs. The circular network (CNET) plot illustrates the genes associated with each GO-terms downregulated in the old vestibular HCs and their interrelationships (Fig.5A, B). We identified many genes linked to ciliopathies, congenital deafness, and balance disorders[47,48,52,53]. Age-related downregulation of genes involved in hair bundles, such as *Ccdc40, Ccdc96, Pifo, Gsn, Cfap126, Hydin, Rpsh1, Ttll3, Ttc21a, Cafp45,* as

well as those linked to HC maintenance such as *Espn, Ush1c, Pou4f3, Homer2, and Slc17a8,* could play a pivotal role in the pathogenesis of ARVD. Concordant with our transcriptomic findings, our experimental validations show a loss of key HC markers at both gene and protein levels (Fig.5C-E). Moreover, our GO analysis supports our observation of the downregulation of numerous genes related to proteostasis such as *Hsp90aa1, Hsp90ab1, Hspa2, Cct7*, and *Dnajb2*. Age-driven dysregulation of proteostasis and subsequent accumulation of protein aggregates lead to the onset of various diseases, including neurodegenerative diseases[54]. ARVD is increasingly recognized as a key player in neurodegenerative diseases and cognitive decline, indicating a bidirectional association[55]. Interestingly, our KEGG pathway analysis of old vestibular HCs revealed a significant enrichment of signaling pathways linked to various neurodegenerative diseases including Alzheimer's (AD), Parkinson's (PD), Huntington's (HD), and amyotrophic lateral sclerosis (ALS) along with an elevation in the expression of AD/PD (*Apoe, App, Mapt*), HD (*Htt*), ALS, and dementia (*Nefl, Fus, Tardbp, C9orf72*) susceptibility genes[56–59](Fig.5F, G). Mapt encodes for microtubule-associated protein Tau. Tau hyperphosphorylation is a biomarker of tauopathies such as AD and PD and is also a prominent hallmark of neuron aging[60]. We immunolabeled vestibular HCs with p-Tau and noted an increase in the p-Tau expression in the old vestibular HCs (Fig.5H). Our results suggest that neurons and vestibular HCs exhibit some shared aging patterns, indicating that vestibular HC aging may represent both an associated condition and a potential risk factor for neurodegenerative diseases. These results further emphasize the complex interplay between universal and cell-type specific mechanisms underlying ARVD and a potential association with neurodegenerative diseases.

Universal and cell-type specific aging signatures in human vestibular HCs

To examine the aging signatures in human vestibular HCs, we utilized scRNA-seq data sets from human organ donors (GSE207817)[61]. Data were pre-processed and clustered using standard scRNA-seq workflow, and clusters were annotated based on known markers. Currently, there are no young human vestibular datasets available. Thus, we used our murine data for comparative analysis via mapping murine and human orthologs as described in the Methods. We observed a 12,873 gene overlap, which was used for the downstream analysis post-mapping (Supplementary Fig.4). We performed a GO analysis to examine the biological pathways downregulated in the human vestibular HCs. Consistent with our murine findings (Fig.3-5), we noted the downregulation of GO-terms related to both cell-type specific and universal aging programs in human HCs (Fig.6A). Analysis of GO term-associated genes revealed similar gene signatures in human vestibular HCs as observed in our murine data (Fig.6B). We noted the downregulation of HC function-related genes including those linked with hearing/balance disorders such as *USH1C, ESPN, ATP2B2, ACTB, CDH23, TMC1, CALM1, FBXO2, TEKT2, CFAP46, CFAP126, CCDC40,* and *CCDC96*. Similar to old murine vestibular HCs, we observed an increase in genes linked to mitochondrial function, antioxidant response and detoxification and a decrease in genes linked to mitochondrial quality control and biogenesis in stress response indicating signs of mitochondrial dysfunction and increased oxidative stress. Next, we assessed age-driven epigenetic changes and noted a reduction in genes linked to global heterochromatin and nucleosome remodeling, changes in histone marks, global DNA hypomethylation, and CpG hypermethylation. Analysis of autophagy revealed an increase in a few genes along with downregulation of numerous genes linked to autophagy initiation, autophagosome formation, autophagosome-lysosomal fusion and mitophagy indicating diminished autophagy and defective mitochondrial elimination. Furthermore, we noted a significant downregulation of various DNA damage repair genes. Evaluation of proteostasis revealed a reduction in genes related to misfolded/unfolded protein response and protein turnover. We observed no significant enrichment in SASP in the human HCs (Supplementary Fig.4D). These findings reveal that the aging signatures observed in human vestibular HCs align closely with those identified in our murine model.

Tissue-specific variations in aging between vestibular and cochlear HCs

Prior studies have highlighted differences in the onset of age-related physiological and morphological changes between the cochlea and vestibule. However, these differences remain poorly understood[9,62]. We conducted auditory brainstem response (ABR), distortion product otoacoustic emissions (DPOAE), and endocochlear potential (EP) to investigate auditory functional decline in our animal cohorts in addition to VsEP (Supplementary Fig. 5A-C). In line with previous studies, we observed a significant elevation in ABR and DPOAE thresholds during aging[63]. Although various studies have reported an age-related decline in EP, our findings revealed no changes in EP. Next, we assessed the age-related morphological changes in the cochlea. Like vestibular type I and II HCs, the cochlea contains two subtypes classified as inner and outer HCs (IHCs and OHCs), which are organized tonotopically along the length of the cochlea. Previous findings indicate that the apical and basal turns of the cochlea, which are responsible for detecting low and high frequencies, respectively, show greater vulnerability to aging[34]. We observed a significant HC loss across the tonotopic organization of the cochlea (Supplementary Fig.5D), while no age-related HC loss was observed in the vestibule (Fig.1). Consistent with previous studies[34], we also noted age-related hypertrophy and atrophy in the cochlear HCs. In particular, we observed atrophy of both IHCs and OHCs in the apical turn, and OHC atrophy and IHC hypertrophy in the basal turn (Supplementary Fig.5E). Next, we assessed tissue-specific variations in aging between vestibular and cochlear HCs at the molecular level (Fig.7). We conducted GO analysis to examine the biological processes downregulated in old cochlear HCs compared to age-matched vestibular HCs. We noted a significant downregulation of HC-specific functions, including sensory perception and response, stereocilia-related processes, and synapsis in cochlear HCs. We also observed the downregulation of universal processes such as oxidative stress, DNA damage, inflammatory response, and diminished proteostasis and autophagy compared to age-matched old vestibular HCs (Fig.7A, Supplementary Fig.4I). Concordant with that, we observed the age-related downregulation of key genes essential for HC function in old cochlear HCs (Fig.7B). Comparison of age-related log2 fold changes in HC-related gene expression in cochlear and vestibular HCs revealed more pronounced downregulation in cochlear HCs compared to vestibular HCs (Fig.7C). Furthermore, we observed a drastic increase in senescence-associated β-galactosidase (SA-β-gal) activity, a major indicator of cellular senescence, in both old cochlear and vestibular HCs (Fig.8E). Unlike young vestibular HCs, we noted the expression of SA-β-gal in young cochlear HCs, indicating early onset of aging in cochlear HCs at the molecular level. These findings highlight tissue-specific aging differences between vestibular and cochlear HCs.

Discussion

Despite the high prevalence of ARVD, the molecular basis is inadequately understood, hindering the development of targeted treatments[3,6,9]. In this study, we conducted a comprehensive transcriptomic analysis alongside functional and morphological assessments to examine age-related alterations in the vestibular end organs in mice. We identified genes and molecular processes associated with both universal and cell-type specific aging signatures in the vestibular HCs. Similar transcriptomic changes were also found in humans, suggesting conserved mechanisms in the two species. In addition, we unveiled tissue-specific variations in the aging between cochlear and vestibular HCs at the molecular level, providing insights into different paces of aging in the two sensory organs in the inner ear.

Aging cells, including post-mitotic neurons, photoreceptor cells, and cochlear HCs, exhibit universal aging hallmarks[2,64–66], and we speculated that vestibular HCs may adhere to these hallmarks. Our data indicated an increase in senescence, marked by a decrease in cyclin-dependent kinases (CDKs), and an increase in cyclin-dependent kinase inhibitors (CDKis) alongside alterations in SASP genes related to laminins, heterochromatic-foci, apoptosis, hypoxia, and angiogenesis in old HCs. This was further evident by elevated SA-β-gal staining in old vestibular HCs (Fig.7). Oxidative stress and inflammation play a critical role in ARHL[67]. Similarly, we noted increased oxidative stress and low-grade inflammation in old vestibular HCs. Mitochondrial electron transport chain (ETC) byproducts are a major

contributor to ROS generation. We observed an age-related increase in multiple ETC genes accompanied by antioxidant genes suggesting increased ROS production and clearance. However, we noted that genes related to H_2O_2 free radical clearance were downregulated, suggesting reduced ROS clearance. Moreover, genes involved in mitochondrial stress response and quality control were elevated, further indicating increased oxidative stress and adaptive mechanisms. While our findings suggested active maintenance of autophagy, several genes involved in autophagosome formation and energy sensing were decreased. We observed an age-related decrease in genes involved in DNA repair mechanisms, indicating diminished DNA damage repair efficiency in old vestibular HCs. Moreover, we noted significant epigenetic alterations with aging, including alterations in histone marks, DNA methylation, global heterochromatin, and nucleosome remodeling. We also noted a significant reduction in genes involved in ECM and intercellular communication, including cadherins, protocadherins, and integrins in the old vestibular HCs. Age-related downregulation of these genes may contribute to the degeneration of tip/lateral links leading to stereocilia fusion (Fig.1). These genes also play a crucial role in cell adhesion, and reduction may lead to an age-related decrease in cell-cell adhesion. This could explain why we obtained a higher yield of isolated HCs from the old vestibular samples compared to young samples (Fig.2). Prior studies show a correlation between neurodegenerative diseases and both ARHL and ARVD[68]. Dysregulated proteostasis plays a crucial role in the accumulation of harmful protein aggregates, leading to neurodegenerative diseases[54]. Omata et al. show that overexpression of β-Amyloid and tau proteins in cochlear HCs of Alzheimer's mouse model indicated severe hearing defects at high frequencies and significant HC loss in basal turn with aging compared to wild-type controls. Interestingly, we observed increased p-Tau accumulation in the vestibular HCs with biological aging alongside the increased expression of neurodegenerative susceptibility genes (Fig.5), suggesting shared aging patterns between neurons and vestibular HCs. While the above findings aligned with our human transcriptomic findings (Fig.5), we did not observe a notable increase in senescence in human HCs (Supplementary Fig.4). This could be due to the relatively young age of the human sample (~45-years), and older samples may reveal enhanced changes.

Due to the multifaceted decline of oculomotor, postural, perceptual, and cognitive functions in ARVD, age-related synaptic and neuron loss has long been considered the major contributor to ARVD. While there are mixed findings on age-related synaptic and vestibular ganglion neuron density, recent reports have shown no significant loss of synapses[3] and vestibular neurons[69] during aging. While our findings indicated some changes, there were no substantial changes in genes related to Ca^{2+} and K^+ channels (Supplementary Fig.4). The most striking age-related changes were observed in the genes associated with the hair bundles and mechanotransduction apparatus (Fig.4,5), which is highly consistent with the age-related stereociliopathy and kinocilia degeneration observed at the morphological level (Fig.1). Interestingly, most of the down-regulated genes, including *Ush1c, Tmc1, Pou4f3, Espn*, *Fbxo2, Atp2b2, Slc17a8, Homer2, Ccdc39, Ccdc40,* and *Tekt2*, are associated with congenital hearing and balance disorders[47,48,53,70]. Owing to the wear and tear theory of aging[71], hair bundles are particularly vulnerable to aging as they are the first in line to respond to mechanical stimuli, causing constant bundle deflection. Unlike the cochlea, where the age-related HC loss is substantial, we observed no vestibular HC loss, consistent with previous studies. Therefore, the age-related vestibular functional decline may not be due to loss of HCs, neurons, or synapses but rather due to deterioration of the hair bundle and mechanotransduction machinery, resulting in diminished sensory perception[6,12,72].

Numerous studies have shown diverse molecular changes in various sensory organs during biological aging. These changes vary based on the inherent differences in cellular dynamics in each organ, which regulate the degree and pace of aging[73,74]. Examination of the aging signatures of old cochlear HCs relative to age-matched vestibular HCs indicated significant downregulation of processes and genes related to cell-type specific (stereocilia, mechanotransduction) and universal programs, aligning with the increased loss of cochlear HCs, bundle, and cellular hypertrophy/atrophy at the morphological level[9,34](Supplementary Fig.) We also noted the early onset of senescence in cochlear

HCs compared to vestibular HCs, as evidenced by SA-β-gal activity in young cochlear HCs (Fig.7). This indicates a relatively slower pace or late onset of aging in vestibular HCs compared to cochlear HCs. While it is difficult to pinpoint a single mechanism that underlies this disparity, we provide molecular evidence to corroborate the presence of a difference in the pace of aging between the cochlear and vestibular HCs. This study has some limitations. Our findings require further investigation utilizing genetic knockout models to examine how these genes impact vestibular function. We assessed the age-related changes in HCs by pooling the HCs from the three vestibular end organs together, which may mask important regional differences in age-related molecular changes. Although the aging signatures of murine findings were mirrored in human data, we utilized our young murine data for comparison due to the lack of young human data sets, and thus, the conclusions require validation using young human specimens.

To the best of our knowledge, this is the first study to comprehensively characterize universal and cell type-specific aging signatures of the vestibular HCs. Both universal and cell-type specific aging mechanisms may likely occur early at the molecular level, causing the gradual accumulation of degenerative changes in the vestibular HCs preceding the morphological and functional decline observed at later stages. Our study provides a comprehensive understanding of the underlying mechanisms and molecular drivers of ARVD highlighting bundle degeneration and subsequent decline in mechanotransduction as a key contributor, providing insights into previously unknown arenas in vestibular aging and highlighting potential biomarkers paving the way to develop targeted treatment strategies to mitigate ARVD.

Methods

Experimental animals

Wild-type male and female CBA/J mice used in this study were purchased from the Jackson Laboratory (Stock #:000656) and were bred and aged in the Animal Facility of Creighton University under standard conditions. The acoustic environment of the animals was examined by a sound level meter (CEL-500, Casella Cel, UK). The sound levels were 68 dB SPL over 98% of the time, and 75 dB SPL 1-2% of the time. All experimental procedures were approved by the Institutional Animal Care and Use Committee of Creighton University.

Vestibular Sensory Evoked Potential (VsEP)

Animal preparation and VsEP testing were performed as previously described[75]. Briefly, mice were anesthetized with a combination of Ketamine (126 mg/kg)/Xylazine (14 mg/kg) injected intraperitoneally and supplemented as needed to maintain the anesthesia. Body temperature was maintained at 37±1ºC via a homeothermic heating blanket. The recording electrodes were placed anterior to the nuchal crest (non-inverting), behind the pinna (inverting), and over the hip (ground) subcutaneously. A custom head clip was used to secure the head to the mechanical shaker (ET-132 Labworks Inc.). The head translation was induced along the naso-occipital axis at a rate of 17 linear pulses per second with alternating polarity and stimulus intensities ranging from +6 to -18 dB relative to 1.0 g/ms (1.0 g = 9.8 m/s^2) adjusted in 3 dB intervals. A broad-band forward masker (50-50,000 Hz, 92 dB SPL) was presented to avoid auditory responses. 128 responses from each of the two polarities (upward and downward head translations) were averaged to yield the mean VsEP response~~s~~. First positive (p1) and negative (n1) response peaks correspond to the compound action potential from the vestibular nerve. Thus, the amplitude and latency of these peaks were quantified. The threshold was defined as the mid-level of the lowest stimulus intensity that elicited a detectable response and the next lowest level that did not produce a detectable response.

Auditory brainstem response (ABR) and Distortion Product otoacoustic emissions (DPOAE)

ABRs were recorded from young and old mice in a soundproof chamber as previously described[34]. The mice were anesthetized with a mixture of ketamine/xylazine and the body temperature was maintained using a heating pad as mentioned in the VsEP procedure. Platinum recording electrodes were placed

422 at the vertex (non-inverting), mastoid prominence (inverting), and leg (ground) subcutaneously. Tone
423 bursts ranging from 4-50 kHz were used as the stimuli, and ABRs were amplified (100,000x), filtered,
424 and recorded by the TDT RZ6 (Tucker-Davis Technologies, Alachua, FL). 200 stimulus repetitions were
425 used to yield the averaged responses. The lowest sound pressure level (dB) at which any wave (wave
426 I to IV) was visibly detected and reproducible above the noise level was regarded as the ABR threshold.
427 The DPOAE at 2f1-2f2 was recorded in response to f1 and f2, with f1/f2=1.2 and the f2 level was set
428 10 dB lower than f1. The sound signal was recorded from the inner ear canal via a microphone,
429 amplified, and the fast Fourier transforms were computed from the averaged waveforms obtained from
430 the inner ear sound signal. The f1 sound pressure required to produce a response above the noise
431 level at the frequency of 2f1-f2 was considered the DPOAE threshold.
432
433 **Endolymphatic potential (ELP) and endocochlear potential (EP)**
434 ELP and EP measurements from the young and old mice were performed as described previously[76].
435 Post anesthesia, tracheotomy was performed in the ventral position without providing artificial
436 respiration. Tissue and musculature overlying the tympanic bulla were removed and bulla was opened
437 to access the cochlea. A fine drill was used to make small holes in the lateral wall in the apical and the
438 basal turns of the cochlea. A glass capillary microelectrode (5-8 MΩ) filled with 150 mM KCl was
439 mounted on the Leica micromanipulator. A stable positive DC potential was observed when
440 microelectrode entered the scala media. The responses were amplified (high-pass filter at 1 kHz) using
441 an Axopatch 200B amplifier (Molecular Probe, Sunnyvale, CA, USA) under current-clamp mode and
442 acquired by software pClamp 10 running on an IBM-compatible computer with 16-bit A/D converter
443 (Digidata 1440A). The voltage changes during the penetration were recorded under the gap-free mode
444 via Clampex in the pClamp software (version 10, Molecular Devices) with a sampling frequency of 1
445 kHz. ELP in the utricle was recorded by inserting the microelectrode through the round window,
446 advanced across scala media, and scala vestibuli to the utricle. The tip of the microelectrode was
447 loaded with fluorescent phalloidin (Invitrogen #565227) diluted in 150 mM KCl (1:100) and injected into
448 the utricle to confirm that the recording was made from the utricle. Post-recording utricle was processed
449 and observed under a confocal microscope.
450
451 **Scanning electron microscopy (SEM)**
452 Utricle and cristae from the two age groups were dissected and fixed in 2% glutaraldehyde, and 4%
453 PFA in 0.1M sodium cacodylate buffer (pH-7.4) overnight. The fixed samples were washed with 0.1 M
454 phosphate buffer. After removing the otolithic membrane from the utricle, the samples were treated with
455 1% Osmium tetroxide and washed with 0.1M sodium cacodylate buffer. The samples were then
456 dehydrated using a series of ethanol, followed by critical point drying using carbon dioxide via critical
457 point dryer (EMS 850) and mounted onto the SEM stubs. The morphology of the stereocilia bundle was
458 visualized and the images were acquired via FEI Quanta 200 scanning electron microscope
459 (ThermoFisher, Hillsboro, OR).
460
461 **Cell dissociation, cDNA library preparation, and single-cell RNA sequencing**
462 Male and female mice aged 2.5 months (young) and 22 months (old) were used for scRNA-seq. Whole
463 cochlear and vestibular organs were microdissected from the inner ears of CBA/J mice in petri dishes
464 containing cold L-15 media (Gibco #11320033). The sensory epithelia were subjected to enzymatic
465 digestion by transferring into 1.5 ml eppendorf tubes containing 1 ml/mg collagenase IV (Sigma) in L-
466 15 medium for 10 minutes at room temperature. Then the cells were resuspended in 400 µL of enzyme-
467 free DMEM containing 10% fetal bovine serum. Single-cell suspensions were obtained by trituration
468 using a trimmed 200 µl pipette tip and filtered with a 40 µM strainer. The cells were pelleted by
469 centrifuging at 300 xg for 5 mins at 4°C, then resuspended in media and subsequently quantified the
470 number of cells. 7-8 mice were used for each biological replicate, and 5 biological replicates were
471 obtained for cochlea and vestibule for the two age groups, respectively. Single-cell capture and library
472 preparation were performed using droplet-based microfluidic technology, following the manufacturer's

instructions for the Chromium Next GEM Single Cell 3' v3.1 dual index kit. The quality of the obtained libraries was assessed via high-sensitivity DNA kits (Agilent Technologies) using Agilent 4200 TapeStation prior to sequencing with Illumina NovaSeq 6000.

Raw data processing and quality control

Standard 10x Genomics CellRanger pipeline (version 6.1.2) was used for demultiplexing, alignment (10x mouse reference genome mm10), barcode processing, and UMI counting to obtain the filtered count matrices. Processing and visualization of the scRNA-seq data from cochlea and vestibule were performed in R (version 4.2.3). Ten filtered count matrices obtained from 10 biological replicates (5 per age group) from cochlear and vestibular samples were loaded into R, converted to Seurat Objects, and pre-processed to eliminate the poor-quality cells using parameters such as counts, features, percentage of mitochondria, ribosomes, and blood gene content. Cells with at least 200 features, 1000 UMI counts, and less than 25% mitochondrial genes were included for the downstream analysis. Individual Seurat Objects were integrated into a single Seurat Object for each age group resulting in two main Seurat Objects for young and old samples in both cochlea and vestibule, respectively, creating four Seurat Objects in total (Supplementary Fig.1).

Normalization, scaling, integration, dimensional reduction, and cluster annotation

Integrated objects were then normalized using log-normalization and scaled using the 'NormalizeData' and 'ScaleData' functions, followed by unsupervised principal component analysis (PCA) and dimensional reduction. First 30 PCs were used for the dimensional reduction. The 'FindNeighbors' was used to calculate pairwise similarities and the 'FindClusters' function which uses the Louvain algorithm was applied with the optimal cluster resolution for all four Seurat Objects respectively. The top markers of each cluster were identified using the 'Findmarkers' function. Samples were then visualized via uniform manifold approximation and projection (UMAP) (Fig.2). This dimensional reduction method uses k-nearest neighbors and Euclidean distance algorithms preserving the local and global structure of the data. A total of 33 and 27 distinct clusters were identified from the initial clustering of young and old vestibular samples, while 31 and 33 clusters were identified from young and old cochlear samples, respectively. Previously reported cell-type-specific pan markers were used to classify the cell-type distribution in young and old vestibular and cochlear samples. Based on the known marker genes, we identified many cell types including vestibular type I and II HCs as well as cochlear IHCs and OHCs. Vestibular and cochlear HC clusters from the two age groups were then subsetted out and reclustered for the downstream analysis to investigate the age-related molecular changes (Supplementary Fig.1). Same method was followed to assess the subclusters within the primary vestibular HC clusters (Supplementary Fig.2, 3).

Pseudobulk gene expression analysis

Subsetted out young and old type I and II HCs were used to extract raw count data from single cells and aggregated them by averaging counts across young and old biological replicates to generate a pseudobulk data frame that contains summed expression values for the 4 HC groups (young and old type I and II). Expression values were then scaled and log2-normalized. Genes associated with universal aging pathways were gathered manually from multiple resources such as Aging Atlas, GenAge, SASP Atlas, and literature. Then the general trends in the age-related expression changes were evaluated using genes associated with each aging pathway using the 'ComplexHeatMap' function. Expression data were extracted and centered using Cluster 3.0 (version 1.59), and heatmaps were generated using JAVA TreeView (version 1.2.1) (Fig.3).

Differentially expressed gene (DEG) analysis

Principle component analysis (PCA) was performed to assess the variance among young and old vestibular datasets by using the 'DESeq2' package in Seurat. The default statistical test in the 'DESeq2' package is the Wald test with Benjamini-Hochberg correction for multiple testing. DESeq2 uses a

generalized linear model (GLM) to identify DEGs within multiple groups, and variance stabilizing transformation (VST) is used to assess the variance revealing the biological patterns in data. DESeq2 pseudo bulk differential expression pipeline was used to generate Venn diagram via ggplot2 based 'ggVennDiagram' package. The Wilcoxon rank-sum test with Bonferroni correction in Seurat was used to assess the differentially expressed genes in young and old samples and subsequently visualized as heatmaps and volcano plots. The top 50 DEGs were identified using the 'FindMarkers' function using young HCs as the reference and old HCs as the test group to generate heatmaps using the 'DoHeatmap' function. The genes at least expressed in 25% of cells in the cluster were considered for this analysis and ordered according to Log2 fold change (Log2FC). The 'EnhancedVolcano' function was used to generate the volcano plots using a fold-change cut-off (FCcutoff) value of 0.25 and a p-value (pCutoff) of 0.05. Some of the DEGs associated with aging signatures were used to generate the ridge plots using the 'RidgePlot' function in Seurat. This plot uses kernel density estimation (KDE) to illustrate the distribution of gene expression levels (Fig.4).

Functional enrichment analysis

The biological relevance of the top DEGs in the old samples compared to the young samples was assessed using gene ontology (GO) enrichment and over-representation analysis. EnrichGO in the 'clusterProfiler' package in Seurat was used to conduct this analysis. This algorithm uses the Hypergeometric test with the Benjamini-Hochberg method for multiple testing corrections. The top genes that were downregulated with aging (Log2FC<0) were used to assess the biological processes (BP), and molecular function (MF). Pairwise semantic similarity was computed for clustering the GO terms and data were visualized as Dot plots, Emap plots, and Cnet plots (Fig.5,6,7). Kyoto Encyclopedia of Genes and Genomes (KEGG) analysis was performed to assess the pathways enriched in old vestibular HCs (Log2FC<0). DESeq2 was used to generate a pseudo bulk data matrix as described above in the DEG analysis. The 'enrichKEGG' function in the 'clusterProfiler' package was used for this analysis. This algorithm also uses the Hypergeometric test with the Benjamini-Hochberg adjustment. For human data sets, before GO analysis, the counts were aggregated to generate a Log2-transformed pseudo bulk matrix. 'biomaRt' package was used to map the Ensemble gene IDs of murine and human orthologs. Only the overlapping genes were used for the downstream analysis. Commonly expressed genes in both mouse and human data were intersected and aggregated into pseudo bulk matrices. Log2 fold changes were calculated for each gene and downregulated genes (log2FC<0) were used for the GO analysis using 'clusterProfiler' package (pvalueCutoff-0.05) as described above.

Histology

Temporal bones were isolated from the young, and old mice, and a hole was made in the apical cochlea followed by overnight fixation with 4% PFA (Electron Microscopy Science, Cat: 15710) in PBS (Cytvia, SH30258.02). Tissues were thoroughly washed with 1x PBS, cleared with xylene, and rehydrated with a series of ethanol. Then tissues were embedded in paraffin wax, and the 8-10 µm thick sections were made using a microtome. H&E staining was performed using Fisher Scientific Gemini™ AS automated slide stainer. The slides were loaded onto the Gemini AS basket and immersed in xylene for 3 minutes (x3), followed by a series of ethanol washes (100%, 95%, and 70%), 2 mins each. Next, the slides were immersed in hematoxylin for 2 mins, rinsed with water, and clarifier two was added (20 seconds) followed by 1 min rinse with water. Bluing reagent was added for 1 min, followed by 1 min water rinse. Slides were then submerged in 70% and 95% ethanol (2 mins each). Then the slides were immersed with counterstain eosin for 1 min and the slides were then immersed in 100% ethanol (2 mins X3) followed by incubation with xylene (2 mins x3) and mounting. Images were taken using Olympus VS120 virtual slide scanner and processed via Olympus VS120 application.

575 **Immunostaining and Confocal imaging**
576 Temporal bones were isolated from the young, and old mice, and a hole was made in the apical cochlea
577 followed by overnight fixation with 4% PFA (Electron Microscopy Science, Cat: 15710) in PBS (Cytvia,
578 SH30258.02) solution at 4°C. The vestibule and cochlea were microdissected from the temporal bones,
579 then permeabilized in 1x PBST (0.1% Triton-X-100 in PBS) for 30 min followed by blocking with 10%
580 normal goat serum for 1h at room temperature. Tissues were incubated with primary antibodies
581 overnight at 4°C on a rocker. The samples were thoroughly washed with 1x PBST for 30 min and
582 incubated for 40 min at room temperature with secondary antibodies and counterstains such as DAPI
583 and Phalloidin. The tissues were subsequently washed with 1x PBST for 40 min and carefully mounted
584 with Fluoromount mounting media. For cryosections, the tissues were fixed overnight with 4% PFA in
585 PBS solution at 4°C and decalcified in 10% EDTA (E671001-0500; Sangon Biotech). Tissues were
586 washed with PBS post-fixing and cryoprotected in a sucrose gradient of 15% and 30%. The sections
587 were then embedded in OCT (Fisher Healthcare, Cat:4585) and kept on dry ice. 10 µm thick sections
588 were made using Cryostat (Leica CM 1950). We used primary antibodies to immunolabel the following
589 markers, anti-ESPN (Protein tech, Cat.20717-1-AP, 1:200), anti-CCDC39 (Sigma Prestige Antibodies,
590 Cat. HPA035564, 1:200), anti-CCDC40 (Sigma Prestige Antibodies, Cat., 1:200), anti-MYO6 (Proteus,
591 Cat. 25-6791, 1:300), anti-MYO7A (Proteus, Cat. 25-6790, 1:300), anti-β-Tubulin (Sigma Millipore, Cat.
592 T6793, 1:200), anti-phospho-tau (gift from Dr. Marisa Zallocchi, 1:200), anti-SOX2 (Invitrogen, Cat.14-
593 9811-82, 1:300), Phalloidin Flour™ 488 (Invitrogen, Cat. A12379, 1:300), Phalloidin Flour™ Plus 405
594 (Invitrogen, Cat. A30104, 1:300). Goat anti-rabbit Fluor 568 (Invitrogen, Cat. A11011,1:300), goat anti-
595 rabbit Fluor 488 (Invitrogen, Cat. A32731, 1:300), goat anti-mouse Fluor 488, Invitrogen, Cat. A11001,
596 1:300) secondary antibodies were used. Confocal images were taken via Zeiss LSM 700 upright
597 microscope, Zeiss LSM 700 inverted microscope, and Nikon-TI-2 Spinning Disk super-resolution
598 confocal microscope. Virtual image sections were captured using Imaris, and Adobe Photoshop was
599 used to remove the background and isolate individual hair cell images.
600
601 **RNAscope *in situ* hybridization**
602 Decalcification and microdissection of young and old vestibular and cochlear tissues were performed
603 as described above in the immunohistochemistry. Gene expression validations were performed using
604 RNAscope *in situ* hybridization following the manufacturer's instructions for RNAscope™ 2.5 HD Red
605 Assay from Advanced Cell Diagnostics (ACD Bio, Cat: 322360). In brief, paraffin-embedded tissue
606 sections of 10 µm were baked in the HybEZ oven at 60°C followed by 10 mins incubation with xylene
607 and ethanol to dewax and dehydrate, respectively. Sections were then subjected to hydrogen peroxide
608 and protease treatment before incubation with probes for 2h at 40°C. Subsequently, amplification,
609 detection, and counterstaining with Dapi were carried out before the samples were mounted. Images
610 were acquired via Zeiss 700 inverted confocal microscope and the obtained z-stacks were presented
611 in maximum-intensity projection. Following this procedure, 10 probes were used to assess the gene
612 expression including *Espn* (Cat. 1061141), *Tmc1* (Cat. 520911), *Atp2b2* (Cat. 1262061), Fbxo2 (Cat.
613 524151), *Pou4f3* (Cat. 1740841), *Homer2* (Cat. 581231), *Gjb2* (Cat. 51881), *Mt1* (Cat. 547711), *Hspb1*
614 (Cat. 488361). The quantification of RNAscope fluorescence intensity was conducted using ImageJ
615 (1.53u). In brief, the channels were separated and projected at maximum intensity. The threshold was
616 adjusted, and the HC layer in the sensory epithelia was selected by specifying the region of interest
617 (ROI). The mean fluorescence intensity was measured, the background was subtracted, normalized to
618 the young group, and statistical significance was analyzed by unpaired t-test using Graph Pad Prism
619 10 (Fig.3 and 5).
620
621 **Senescence-associated beta-gal (SA-β-gal) staining and imaging**
622 According to the user manual, senescence-associated beta-gal (SA-β-gal) staining was performed
623 using Cell Signaling #9860 staining kit. The temporal bones were dissected from young and old mice
624 and fixed in the 1X fixative solution provided in the kit for 30 minutes, as previously described[77]. The

whole mounts were incubated in 1x staining solution overnight at 37°C. Samples were mounted and imaged using Olympus VS120 virtual slide scanner (Fig.7).

Statistics and reproducibility

All statistical analyses were conducted using the R (v 4.2.3) and Graph Pad Prism 10. The experiments were not randomized and the investigators were not blinded during the data analysis. P-value of <0.05 was considered statistically significant and data was shown as mean ± SD.

Data availability

All relevant data are included in this article, and supplementary information. The single-cell RNA sequencing data generated in this study have been deposited in NCBI Gene Expression Omnibus (GEO) under the accession numbers GSE283534 (young CBA/J) and GSE283708 (old CBA/J).

Code availability

Publicly available standard packages and algorithms were used for the analysis of our sequencing data and no custom code or algorithms were generated. R Markdown can be provided upon request.

Acknowledgment

We thank Dr. Marisa Zallocchi for generously sharing the reagents. This research partially utilized the Auditory and Vestibular Technology (AVT) core (grants GM103427, GM139762), Histology and Molecular core facility (grants RRID:SCR_025163), Department of Chemistry & Biochemistry (EPSCoR) at Creighton University, and DNA Sequencing Core Facility at the University of Nebraska (grant RR018788).

Funding

This work was supported by the National Institute on Deafness and other Communication Disorders (NIDCD), National Institute of Health (R01 DC016807) to D.H. and Dr. Richard. J. Bellucci Pre-doctoral research award to S.K. by Bellucci De Paoli Family Foundation and Creighton School of Medicine.

Author Contributions

S.K., D.H., L.T., B.K. designed the study, S.V., D.H., H.L. performed electrophysiology, D.H., H.L. isolated the inner ear tissues, S.T., M.Z. prepared the sequencing library, S.K., C.B., performed the transcriptomic analysis, S.K., H.L., D.H., B.J.B., performed experiments and quantifications. S.K. prepared the original manuscript and figures, and D.H. and B.K. edited the manuscript.

Declaration of interests

All authors declare no competing interests.

References

1. López-Otín, C., Blasco, M. A., Partridge, L., Serrano, M. & Kroemer, G. The hallmarks of aging. *Cell* vol. 153 1194 Preprint at https://doi.org/10.1016/j.cell.2013.05.039 (2013).
2. López-Otín, C., Blasco, M. A., Partridge, L., Serrano, M. & Kroemer, G. Hallmarks of aging: An expanding universe. *Cell* vol. 186 243–278 Preprint at https://doi.org/10.1016/j.cell.2022.11.001 (2023).
3. Paplou, V. G., Schubert, N. M. A., van Tuinen, M., Vijayakumar, S. & Pyott, S. J. Functional, Morphological and Molecular Changes Reveal the Mechanisms Associated with Age-Related Vestibular Loss. *Biomolecules* **13**, (2023).
4. Bowl, M. R. & Dawson, S. J. Age-related hearing loss. *Cold Spring Harb Perspect Med* **9**, (2019).
5. Schuknecht, H. F. Presbycusis. *Laryngoscope* **65**, 402–419 (1955).
6. Zalewski, C. K. Aging of the Human Vestibular System. *Semin Hear* **36**, 175–196 (2015).
7. Rosenhall, U. & Rubin, W. Degenerative changes in the human vestibular sensory epithelia. *Acta Otolaryngol* **79**, 67–80 (1975).
8. Ji, L. & Zhai, S. Aging and the peripheral vestibular system. *Journal of Otology* vol. 13 138–140 Preprint at https://doi.org/10.1016/j.joto.2018.11.006 (2018).
9. Paplou, V., Schubert, N. M. A. & Pyott, S. J. Age-Related Changes in the Cochlea and Vestibule: Shared Patterns and Processes. *Frontiers in Neuroscience* vol. 15 Preprint at https://doi.org/10.3389/fnins.2021.680856 (2021).
10. Arshad, Q. & Seemungal, B. M. Age-related vestibular loss: Current understanding and future research directions. *Frontiers in Neurology* vol. 7 Preprint at https://doi.org/10.3389/fneur.2016.00231 (2016).
11. Iwasaki, S. & Yamasoba, T. Dizziness and imbalance in the elderly: Age-related decline in the vestibular system. *Aging and Disease* vol. 6 38–47 Preprint at https://doi.org/10.14336/AD.2014.0128 (2015).
12. Fetter, M. Vestibular System Disorders. in *Encyclopedia of Life Sciences* (Wiley, 2010). doi:10.1002/9780470015902.a0002213.pub2.
13. Gillespie, P. G. & Müller, U. Mechanotransduction by Hair Cells: Models, Molecules, and Mechanisms. *Cell* vol. 139 33–44 Preprint at https://doi.org/10.1016/j.cell.2009.09.010 (2009).
14. Lindeman, H. H. Regional Differences in Structure of the Vestibular Sensory Regions. *J Laryngol Otol* **83**, 1–17 (1969).
15. EATOCK, R. A. & HUTZLER, M. J. Ionic Currents of Mammalian Vestibular Hair Cells. *Ann N Y Acad Sci* **656**, 58–74 (1992).
16. Merchant, S. N., Tsuji, K., Veläzquez-Villasenor, L., Glynn, R. J. & Rauch, S. D. *TEMPORAL BONE STUDIES OF THE HUMAN PERIPHERAL VESTIBULAR SYSTEM 1. NORMATIVE VESTIBULAR HAIR CELL DATA*. *Ann Otol Rhinol Laryngol* vol. 109 (2000).
17. Brosel, S., Laub, C., Averdam, A., Bender, A. & Elstner, M. Molecular aging of the mammalian vestibular system. *Ageing Research Reviews* vol. 26 72–80 Preprint at https://doi.org/10.1016/j.arr.2015.12.007 (2016).
18. Sloane, P. D., Baloh, R. W. & Honrubia, V. The vestibular system in the elderly: Clinical implications. *Am J Otolaryngol* **10**, 422–429 (1989).
19. Rosenhall, U. Degenerative patterns in the aging human vestibular neuro-epithelia. *Acta Otolaryngol* **76**, 208–220 (1973).
20. Frisina, R. D. *et al.* F1 (CBA×C57) mice show superior hearing in old age relative to their parental strains: Hybrid vigor or a new animal model for 'Golden Ears'? *Neurobiol Aging* **32**, 1716–1724 (2011).
21. Sha, S. H. *et al.* Age-related auditory pathology in the CBA/J mouse. *Hear Res* **243**, 87–94 (2008).
22. Jones, T. A. *et al.* The adequate stimulus for mammalian linear vestibular evoked potentials (VsEPs). *Hear Res* **280**, 133–140 (2011).

23. Mock, B., Jones, T. A. & Jones, S. M. Gravity receptor aging in the CBA/CAJ strain: A comparison to auditory aging. *JARO - Journal of the Association for Research in Otolaryngology* **12**, 173–183 (2011).
24. Leng, G. *T~I DAVIS THEORY: A REVIEW, AND IMPLICATIONS OF RECENT ELECTROP~SIO~ICAL EVIDENCE*. (1980).
25. Wangemann, P. *HF.ARII RES[ARCH Comparison of Ion Transport Mechanisms between Vestibular Dark Cells and Strial Marginal Cells*. *Hearing Research* vol. 90 (1995).
26. Köppl, C., Wilms, V., Russell, I. J. & Nothwang, H. G. Evolution of Endolymph Secretion and Endolymphatic Potential Generation in the Vertebrate Inner Ear. *Brain, Behavior and Evolution* vol. 92 1–31 Preprint at https://doi.org/10.1159/000494050 (2018).
27. Li, Y., Liu, H., Zhao, X. & He, D. Z. Endolymphatic Potential Measured From Developing and Adult Mouse Inner Ear. *Front Cell Neurosci* **14**, (2020).
28. Merchant, S. N., Tsuji, K., Veläzquez-Villasenor, L., Glynn, R. J. & Rauch, S. D. *TEMPORAL BONE STUDIES OF THE HUMAN PERIPHERAL VESTIBULAR SYSTEM 1. NORMATIVE VESTIBULAR HAIR CELL DATA*. *Ann Otol Rhinol Laryngol* vol. 109 (2000).
29. Rauch, S. D., Velazquez-Villaseñor, L., Dimitri, P. S. & Merchant, S. N. Decreasing hair cell counts in aging humans. in *Annals of the New York Academy of Sciences* vol. 942 220–227 (New York Academy of Sciences, 2001).
30. Gopen, Q., Lopez, I., Ishiyama, G., Baloh, R. W. & Ishiyama, A. *Unbiased Stereologic Type I and Type II Hair Cell Counts in Human Utricular Macula*. (2003).
31. Lu, J. *et al.* Increased Type I and Decreased Type II Hair Cells after Deletion of Sox2 in the Developing Mouse Utricle. *Neuroscience* **422**, 146–160 (2019).
32. Stone, J. S., Pujol, R., Nguyen, T. B. & Cox, B. C. The transcription factor sox2 is required to maintain the cell type-specific properties and innervation of type II vestibular hair cells in adult mice. *Journal of Neuroscience* **41**, 6217–6233 (2021).
33. Boëda, B., Weil, D. & Petit, C. A specific promoter of the sensory cells of the inner ear defined by transgenesis. *Hum Mol Genet* **10**, 1581–1589 (2001).
34. Liu, H. *et al.* Molecular and cytological profiling of biological aging of mouse cochlear inner and outer hair cells. *Cell Rep* **39**, (2022).
35. Finch, C. E. Neuron atrophy during aging: programmed or sporadic? *Trends Neurosci* **16**, 104–110 (1993).
36. Luecken, M. D. & Theis, F. J. Current best practices in single-cell RNA-seq analysis: a tutorial. *Mol Syst Biol* **15**, (2019).
37. Burns, J. C., Kelly, M. C., Hoa, M., Morell, R. J. & Kelley, M. W. Single-cell RNA-Seq resolves cellular complexity in sensory organs from the neonatal inner ear. *Nat Commun* **6**, (2015).
38. McInturff, S., Burns, J. C. & Kelley, M. W. Characterization of spatial and temporal development of Type I and Type II hair cells in the mouse utricle using new cell-type-specific markers. *Biol Open* **7**, (2018).
39. Liu, H. *et al.* Characterization of transcriptomes of cochlear inner and outer hair cells. *Journal of Neuroscience* **34**, 11085–11095 (2014).
40. Campisi, J., Andersen, J. K., Kapahi, P. & Melov, S. Cellular senescence: A link between cancer and age-related degenerative disease? *Seminars in Cancer Biology* vol. 21 354–359 Preprint at https://doi.org/10.1016/j.semcancer.2011.09.001 (2011).
41. Lee, J. H., Kim, E. W., Croteau, D. L. & Bohr, V. A. Heterochromatin: an epigenetic point of view in aging. *Experimental and Molecular Medicine* vol. 52 1466–1474 Preprint at https://doi.org/10.1038/s12276-020-00497-4 (2020).
42. Tadros, S. F., D'Souza, M., Zhu, X. & Frisina, R. D. Gene expression changes for antioxidants pathways in the mouse cochlea: Relations to age-related hearing deficits. *PLoS One* **9**, (2014).
43. Dodson, K. M. *et al.* Vestibular dysfunction in DFNB1 deafness. *Am J Med Genet A* **155**, 993–1000 (2011).

44. Dai, H., Wang, L., Li, L., Huang, Z. & Ye, L. Metallothionein 1: A New Spotlight on Inflammatory Diseases. *Frontiers in Immunology* vol. 12 Preprint at https://doi.org/10.3389/fimmu.2021.739918 (2021).
45. Sun, G. *et al.* Single-cell transcriptomic atlas of mouse cochlear aging. *Protein Cell* **14**, 180–201 (2023).
46. Smits, J. J. *et al.* De novo and inherited loss-of-function variants of ATP2B2 are associated with rapidly progressive hearing impairment. *Hum Genet* **138**, 61–72 (2019).
47. Naz, S. *et al.* Mutations of ESPN cause autosomal recessive deafness and vestibular dysfunction. *J Med Genet* **41**, 591–595 (2004).
48. Pan, B. *et al.* Gene therapy restores auditory and vestibular function in a mouse model of Usher syndrome type 1c. *Nat Biotechnol* **35**, 264–272 (2017).
49. McFadden, J. R. *et al.* Clinical, genetic, and structural characterization of a novel TUBB4B tubulinopathy. *Mol Genet Metab Rep* **36**, (2023).
50. Castiglione, A. & Möller, C. Usher Syndrome. *Audiology Research* vol. 12 42–65 Preprint at https://doi.org/10.3390/audiolres12010005 (2022).
51. Perrin, B. J., Sonnemann, K. J. & Ervasti, J. M. β-Actin and γ-Actin are each dispensable for auditory hair cell development but required for stereocilia maintenance. *PLoS Genet* **6**, 1–12 (2010).
52. Patir, A. *et al.* The transcriptional signature associated with human motile cilia. *Sci Rep* **10**, (2020).
53. Aprea, I. *et al.* Pathogenic gene variants in CCDC39, CCDC40, RSPH1, RSPH9, HYDIN, and SPEF2 cause defects of sperm flagella composition and male infertility. *Front Genet* **14**, (2023).
54. Hipp, M. S., Park, S. H. & Hartl, U. U. Proteostasis impairment in protein-misfolding and -aggregation diseases. *Trends in Cell Biology* vol. 24 506–514 Preprint at https://doi.org/10.1016/j.tcb.2014.05.003 (2014).
55. Coto, J. *et al.* Peripheral vestibular system: Age-related vestibular loss and associated deficits. *Journal of Otology* vol. 16 258–265 Preprint at https://doi.org/10.1016/j.joto.2021.06.001 (2021).
56. Green, G. S. *et al.* Cellular communities reveal trajectories of brain ageing and Alzheimer's disease. *Nature* (2024) doi:10.1038/s41586-024-07871-6.
57. Leavitt, B. R., Kordasiewicz, H. B. & Schobel, S. A. Huntingtin-Lowering Therapies for Huntington Disease: A Review of the Evidence of Potential Benefits and Risks. *JAMA Neurology* vol. 77 764–772 Preprint at https://doi.org/10.1001/jamaneurol.2020.0299 (2020).
58. Taymans, J. M. & Cookson, M. R. Mechanisms in dominant parkinsonism: The toxic triangle of LRRK2, α-synuclein, and tau. *BioEssays* **32**, 227–235 (2010).
59. Leblond, C. S., Kaneb, H. M., Dion, P. A. & Rouleau, G. A. Dissection of genetic factors associated with amyotrophic lateral sclerosis. *Experimental Neurology* vol. 262 91–101 Preprint at https://doi.org/10.1016/j.expneurol.2014.04.013 (2014).
60. Avila, J., Gomez De Barreda, E., Pallas-Bazarra, N. & Hernandez, F. Tau and Neuron Aging.
61. Wang, T. *et al.* Single-cell transcriptomic atlas reveals increased regeneration in diseased human inner ear balance organs. *Nat Commun* **15**, (2024).
62. Arslan, M. The Senescence of the Vestibular Apparatus _ Practica Oto-Rhino-Laryngologica _ Karger Publishers. *Practica Oto Rhino Laryngologica* (1956).
63. Jones, S. M. *et al.* A comparison of vestibular and auditory phenotypes in inbred mouse strains. *Brain Res* **1091**, 40–46 (2006).
64. Sun, G. *et al.* Single-cell transcriptomic atlas of mouse cochlear aging. *Protein Cell* **14**, 180–201 (2023).
65. Liu, H. *et al.* Molecular and cytological profiling of biological aging of mouse cochlear inner and outer hair cells. *Cell Rep* **39**, (2022).
66. Cvekl, A. & Vijg, J. Aging of the eye: Lessons from cataracts and age-related macular degeneration. *Ageing Research Reviews* vol. 99 Preprint at https://doi.org/10.1016/j.arr.2024.102407 (2024).

67. Fujimoto, C. & Yamasoba, T. Oxidative stresses and mitochondrial dysfunction in age-related hearing loss. *Oxidative Medicine and Cellular Longevity* vol. 2014 Preprint at https://doi.org/10.1155/2014/582849 (2014).
68. Previc, F. H. Vestibular loss as a contributor to Alzheimer's disease. *Med Hypotheses* **80**, 360–367 (2013).
69. Wan, G. *et al.* Synaptopathy as a mechanism for age-related vestibular dysfunction in mice. *Front Aging Neurosci* **11**, (2019).
70. Smits, J. J. *et al.* De novo and inherited loss-of-function variants of ATP2B2 are associated with rapidly progressive hearing impairment. *Hum Genet* **138**, 61–72 (2019).
71. Rzadzinska, A. K., Schneider, M. E., Davies, C., Riordan, G. P. & Kachar, B. An actin molecular treadmill and myosins maintain stereocilia functional architecture and self-renewal. *Journal of Cell Biology* **164**, 887–897 (2004).
72. Zwergal, A., Grabova, D. & Schöberl, F. Vestibular contribution to spatial orientation and navigation. *Current Opinion in Neurology* vol. 37 52–58 Preprint at https://doi.org/10.1097/WCO.0000000000001230 (2024).
73. Yamamoto, R. *et al.* Tissue-specific impacts of aging and genetics on gene expression patterns in humans. *Nat Commun* **13**, (2022).
74. Jin, K. *et al.* Brain-wide cell-type-specific transcriptomic signatures of healthy ageing in mice. *Nature* (2025) doi:10.1038/s41586-024-08350-8.
75. Vijayakumar, S. *et al.* Rescue of peripheral vestibular function in Usher syndrome mice using a splice-switching antisense oligonucleotide. *Hum Mol Genet* **26**, 3482–3494 (2017).
76. Li, Y., Liu, H., Zhao, X. & He, D. Z. Endolymphatic Potential Measured From Developing and Adult Mouse Inner Ear. *Front Cell Neurosci* **14**, (2020).
77. Benkafadar, N. *et al.* ROS-Induced Activation of DNA Damage Responses Drives Senescence-Like State in Postmitotic Cochlear Cells: Implication for Hearing Preservation. *Mol Neurobiol* **56**, 5950–5969 (2019).
78. Chou, S. W. *et al.* Fascin 2b is a component of stereocilia that lengthens actin-based protrusions. *PLoS One* **6**, (2011).
79. Jensen-Smith, H. C., Ludueña, R. F. & Hallworth, R. *Requirement for the β I and β IV Tubulin Isotypes In Mammalian Cilia*.
80. Scheibinger, M. *et al.* Cell-type identity of the avian utricle. *Cell Rep* **40**, (2022).

Figure 1

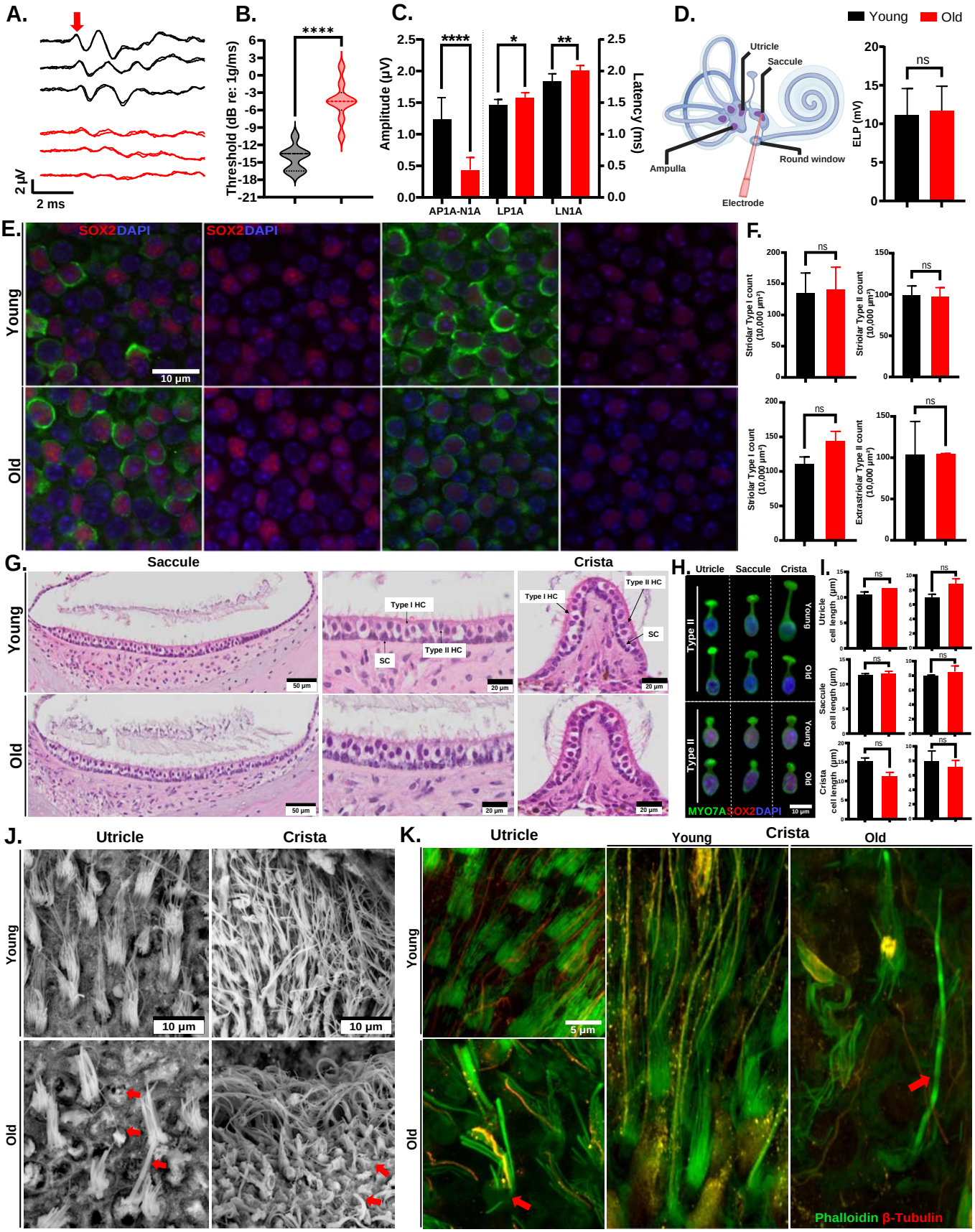
A.
2 µV
2 ms
B.
****
Threshold (dB re: 1g/ms)
C.
****
*
**
Amplitude (µV)
Latency (ms)
AP1A-N1A
LP1A
LN1A
D.
Young
Old
Utricle
Saccule
Ampulla
Round window
Electrode
ELP (mV)
ns
E.
SOX2DAPI
Young
Old
10 µm
F.
Striolar Type I count (10,000 µm²)
Striolar Type II count (10,000 µm²)
Extrastriolar Type II count (10,000 µm²)
ns
G.
Saccule
Crista
Type I HC
Type II HC
SC
50 µm
20 µm
H.
Utricle
Saccule
Crista
Type II
Young
Old
MYO7A SOX2DAPI
10 µm
I.
Utricle cell length (µm)
Saccule cell length (µm)
Crista cell length (µm)
ns
J.
Utricle
Crista
Young
Old
10 µm
K.
Utricle
Crista
Young
Old
5 µm
Phalloidin β-Tubulin

Figure 1: Age-related functional and cellular alterations in the vestibular HCs. **A-C.** The vestibular sensory evoked potential (VsEP) test shows an age-related reduction in the response amplitude (red arrow) (A), the elevation of the threshold (B), and an increase in the latency (C), indicating vestibular functional decline with aging (n = 8-11/age group). **D.** Graphical illustration of inserting the glass capillary microelectrode through the round window of the cochlea to the saccule during vestibular endolymphatic potential (ELP) test (D), and ELP measurement quantifications (n=6/age group). The illustration was created using BioRender. **E.** Representative images of young and old striolar and extrastriolar sensory epithelia from utricle whole mounts immunolabeled with anti-MYO7A, anti-SOX2, and DAPI. **F.** Quantification of type I and II HC density in striolar and extrastriolar regions, respectively (n=2/age group). **G.** Representative images of young and old H&E sections indicating type I and II HCs and supporting cells (SCs) from saccule and crista. **H.** Confocal virtual sectioning images of some individual HCs demonstrating cellular hypertrophy (elongation) and atrophy (shortening) in the three vestibular end organs. **I.** Quantification of HC cell lengths in the three vestibular end organs from histological analysis (n=2/age group). **J.** Scanning electron micrographs indicating stereocilia bundle loss and fusion with aging. **K.** High-resolution confocal microscopic images of actin-rich stereocilia[78] stained with Phalloidin, and microtubule-based[79] kinocilia immunolabeled with β-tubulin indicating stereocilia bundle loss, fusion, and kinocilia degeneration with aging (red arrows). P-values were calculated by 2-way ANOVA multiple comparisons and unpaired t-test (*<0.05, **<0.01, ***<0.001, ****<0.0001, ns - non-significant).

Figure 2

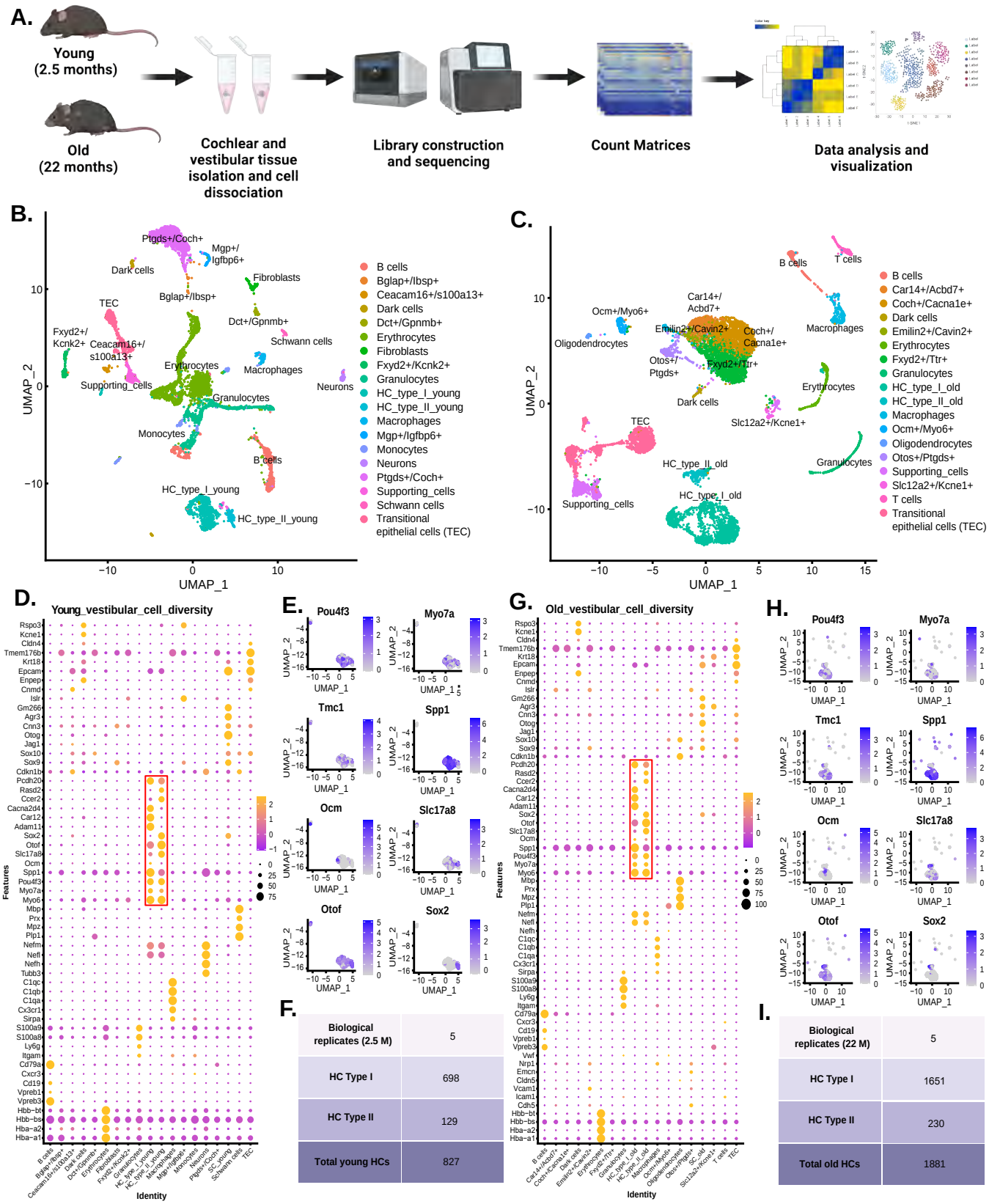
A.
Young (2.5 months)
Old (22 months)
Cochlear and vestibular tissue isolation and cell dissociation
Library construction and sequencing
Count Matrices
Data analysis and visualization
B.
UMAP_1
UMAP_2
B cells
Bglap+/Ibsp+
Ceacam16+/s100a13+
Dark cells
Dct+/Gpnmb+
Erythrocytes
Fibroblasts
Fxyd2+/Kcnk2+
Granulocytes
HC_type_I_young
HC_type_II_young
Macrophages
Mgp+/Igfbp6+
Monocytes
Neurons
Ptgds+/Coch+
Supporting_cells
Schwann cells
Transitional epithelial cells (TEC)
C.
B cells
Car14+/Acbd7+
Coch+/Cacna1e+
Dark cells
Emilin2+/Cavin2+
Erythrocytes
Fxyd2+/Ttr+
Granulocytes
HC_type_I_old
HC_type_II_old
Macrophages
Ocm+/Myo6+
Oligodendrocytes
Otos+/Ptgds+
Supporting_cells
Slc12a2+/Kcne1+
T cells
Transitional epithelial cells (TEC)
D.
Young_vestibular_cell_diversity
Features
Identity
E.
Pou4f3
Myo7a
Tmc1
Spp1
Ocm
Slc17a8
Otof
Sox2
F.
Biological replicates (2.5 M) 5
HC Type I 698
HC Type II 129
Total young HCs 827
G.
Old_vestibular_cell_diversity
Features
Identity
H.
Pou4f3
Myo7a
Tmc1
Spp1
Ocm
Slc17a8
Otof
Sox2
I.
Biological replicates (22 M) 5
HC Type I 1651
HC Type II 230
Total old HCs 1881

Figure 2: Young (2.5M) and old (22M) vestibular cell type distribution. **A.** An illustration of the experimental workflow of scRNA-sequencing including isolation of vestibular and cochlear tissues from the two CBA/J cohorts via microdissection, library construction by 10x Genomics chromium platform, sequencing, conversion of raw sequencing data (Fastq) to count matrices by Cell Ranger (version 6.1.2), followed by downstream quality control, data analysis and visualization by R (version 4.2.3) (Supplementary Fig.1). The illustration was created using BioRender. **B, C.** Uniform manifold approximation and projection (UMAP) plot showing the distribution of different cell types in young and old vestibular samples, respectively. This dimensional reduction method uses k-nearest neighbors (KNN) and the Euclidean distance algorithm to construct a low-dimensional graph for visualization. **D, G.** Dot plots indicating the expression of known marker genes used to identify the cell types and subsequent cluster annotation shown in B and C. The dot size represents the percentage of cells expressing the genes from each cluster, whereas the color indicates the expression level. Expression levels are normalized via z-score normalization. Thus, the average expression is zero, and positive or negative values indicate expression above or below average. **E, H.** Feature plots demonstrating the HC-specific pan marker gene expression in the HC clusters identified in the UMAPs. **F, I.** Number of type I and II HCs identified from young and old vestibular samples for the downstream analysis. 7-8 mice were used per biological replicate, and a total of 5 biological replicates were used for the transcriptomic analysis.

Figure 3

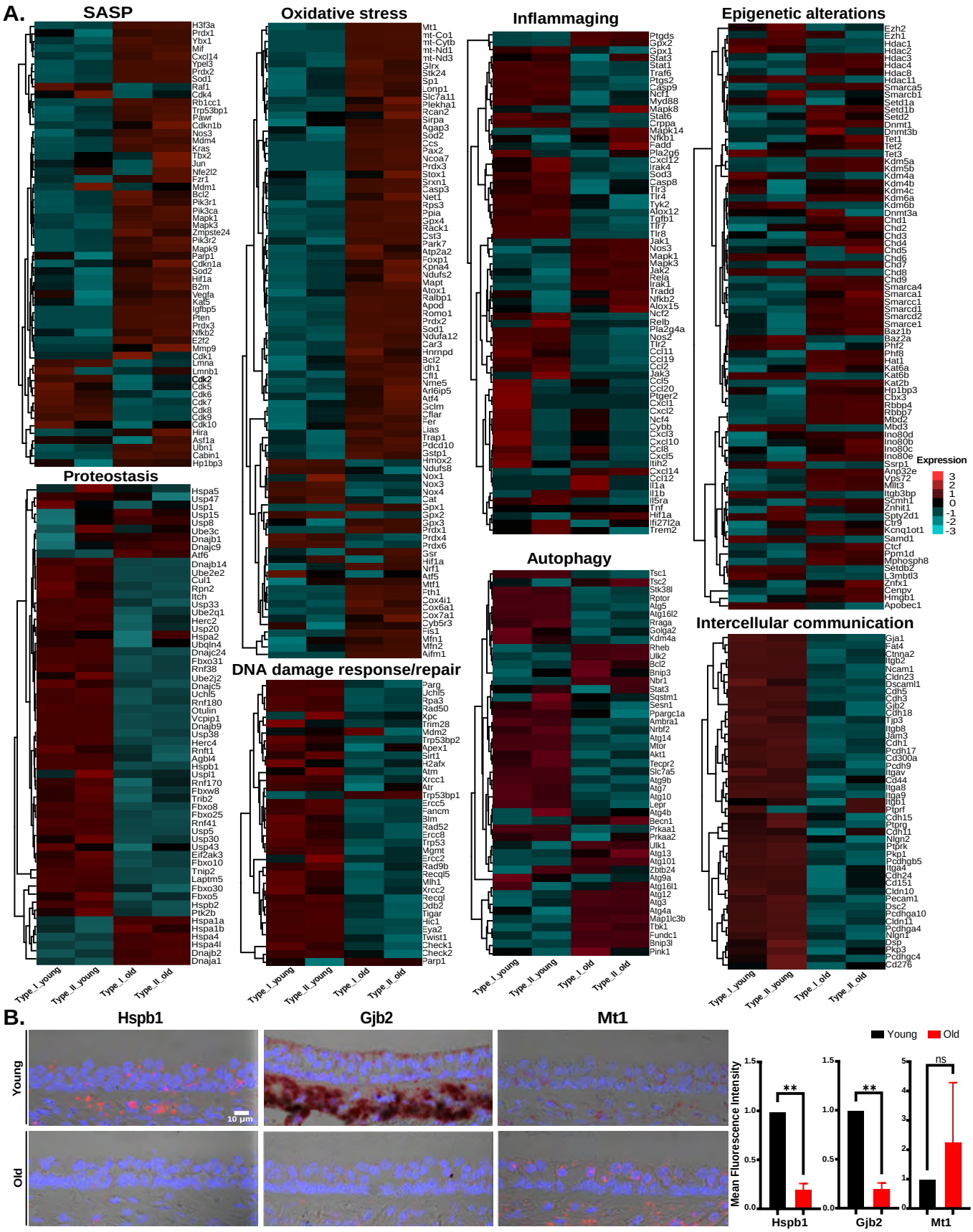
A.
SASP
H3f3a
Prdx1
Ybx1
Mif
Cxcl14
Ypel3
Prdx2
Sod1
Raf1
Cdk4
Rb1cc1
Trp53bp1
Pawr
Cdkn1b
Nos3
Mdm4
Kras
Tbx2
Jun
Nfe2l2
Fzr1
Mdm1
Bcl2
Pik3r1
Pik3ca
Mapk1
Mapk3
Zmpste24
Pik3r2
Mapk9
Parp1
Cdkn1a
Sod2
Hif1a
B2m
Vegfa
Kat5
Igfbp5
Pten
Prdx3
Nfkb2
E2f2
Mmp9
Cdk1
Lmna
Lmnb1
Cdk2
Cdk5
Cdk6
Cdk7
Cdk8
Cdk9
Cdk10
Hira
Asf1a
Ubn1
Cabin1
Hp1bp3
Proteostasis
Hspa5
Usp47
Usp1
Usp15
Usp8
Ube3c
Dnajb1
Dnajc9
Atf6
Dnajb14
Ube2e2
Cul1
Rpn2
Itch
Usp33
Ube2q1
Herc2
Usp20
Hspa2
Ubqln4
Dnajc24
Fbxo31
Rnf38
Ube2j2
Dnajc5
Uchl5
Rnf180
Otulin
Vcpip1
Dnajb9
Usp38
Herc4
Rnft1
Agbl4
Hspb1
Uspl1
Rnf170
Fbxw8
Trib2
Fbxo8
Fbxo25
Rnf41
Usp5
Usp30
Usp43
Eif2ak3
Fbxo10
Tnip2
Laptm5
Fbxo30
Fbxo5
Hspb2
Ptk2b
Hspa1a
Hspa1b
Hspa4
Hspa4l
Dnajb2
Dnaja1
Type_I_young
Type_II_young
Type_I_old
Type_II_old
Oxidative stress
Mt1
mt-Co1
mt-Cytb
mt-Nd1
mt-Nd3
Glrx
Stk24
Sp1
Lonp1
Slc7a11
Plekha1
Rcan2
Sirpa
Agap3
Sod2
Ccs
Pax2
Ncoa7
Prdx3
Stox1
Srxn1
Casp3
Net1
Rps3
Ppia
Gpx4
Rack1
Cst3
Park7
Atp2a2
Foxp1
Kpna4
Ndufs2
Mapt
Atox1
Ralbp1
Apod
Romo1
Prdx2
Sod1
Ndufa12
Car3
Hnrnpd
Bcl2
Idh1
Cfl1
Nme5
Arl6ip5
Atf4
Sclm
Cflar
Fer
Lias
Trap1
Pdcd10
Gstp1
Hmox2
Ndufs8
Nox1
Nox3
Nox4
Cat
Gpx1
Gpx2
Gpx3
Prdx1
Prdx4
Prdx6
Gsr
Hif1a
Nrf1
Atf5
Mtf1
Eth1
Cox4i1
Cox6a1
Cox7a1
Cyb5r3
Fis1
Mfn1
Mfn2
Aifm1
DNA damage response/repair
Parg
Uchl5
Rpa3
Rad50
Xpc
Trim28
Mdm2
Trp53bp2
Apex1
Sirt1
H2afx
Atm
Xrcc1
Atr
Trp53bp1
Ercc5
Fancm
Blm
Rad52
Ercc8
Trp53
Mgmt
Ercc2
Rad9b
Recql5
Mlh1
Xrcc2
Recql
Ddb2
Tigar
Hic1
Eya2
Twist1
Check1
Check2
Parp1
Inflammaging
Ptgds
Gpx2
Gpx1
Stat3
Stat1
Traf6
Ptgs2
Casp9
Ncf1
Myd88
Mapk8
Stat6
Crppa
Mapk14
Nfkb1
Fadd
Pla2g6
Cxcl12
Irak4
Sod3
Casp8
Tlr3
Tlr4
Tyk2
Alox12
Tgfb1
Tlr7
Tlr8
Jak1
Nos3
Mapk1
Mapk3
Jak2
Rela
Irak1
Tradd
Nfkb2
Alox15
Ncf2
Relb
Pla2g4a
Nos2
Tlr2
Ccl11
Ccl19
Ccl2
Jak3
Ccl5
Ccl20
Ptger2
Cxcl1
Cxcl2
Ncf4
Cybb
Cxcl3
Cxcl10
Ccl8
Cxcl5
Itih2
Cxcl14
Ccl12
Il1a
Il1b
Il5ra
Tnf
Hif1a
Ifi27l2a
Trem2
Autophagy
Tsc1
Tsc2
Stk38l
Rptor
Atg5
Atg16l2
Rraga
Golga2
Kdm4a
Rheb
Ulk2
Bcl2
Bnip3
Nbr1
Stat3
Sqstm1
Sesn1
Ppargc1a
Ambra1
Nrbf2
Atg14
Mtor
Akt1
Tecpr2
Slc7a5
Atg9b
Atg7
Atg10
Lepr
Atg4b
Becn1
Prkaa1
Prkaa2
Ulk1
Atg13
Atg101
Zbtb24
Atg9a
Atg16l1
Atg12
Atg3
Atg4a
Map1lc3b
Tbk1
Fundc1
Bnip3l
Pink1
Epigenetic alterations
Ezh2
Ezh1
Hdac1
Hdac2
Hdac3
Hdac4
Hdac8
Hdac11
Smarca5
Smarcb1
Setd1a
Setd1b
Setd2
Dnmt1
Dnmt3b
Tet1
Tet2
Tet3
Kdm5a
Kdm5b
Kdm4a
Kdm4b
Kdm4c
Kdm6a
Kdm6b
Dnmt3a
Chd1
Chd2
Chd3
Chd4
Chd5
Chd6
Chd7
Chd8
Chd9
Smarca4
Smarca1
Smarcc1
Smarcd1
Smarcd2
Smarce1
Baz1b
Baz2a
Phf2
Phf8
Hat1
Kat6a
Kat6b
Kat2b
Hp1bp3
Cbx3
Rbbp4
Rbbp7
Mbd2
Mbd3
Ino80d
Ino80b
Ino80c
Ino80e
Ssrp1
Anp32e
Vps72
Mllt3
Itgb3bp
Scmh1
Znhit1
Spty2d1
Ctr9
Konq1ot1
Samd1
Ctcf
Ppm1d
Mphosph8
Setdb2
L3mbtl3
Znfx1
Cenpv
Hmgb1
Apobec1
Expression
3
2
1
0
-1
-2
-3
Intercellular communication
Gja1
Fat4
Ctnna2
Itgb2
Ncam1
Cldn23
Dscaml1
Cdh5
Cdh3
Gjb2
Cdh18
Tjp3
Itgb8
Jam3
Cdh1
Pcdh17
Cd300a
Pcdh9
Itgav
Cd44
Itga8
Itga9
Itgb1
Ptprf
Cdh15
Ptprg
Cdh11
Nlgn2
Ptprk
Pkp1
Pcdhgb5
Itga4
Cdh24
Cd151
Cldn10
Pecam1
Dsc2
Pcdhga10
Cldn11
Pcdhga4
Nlgn1
Dsp
Pkp3
Pcdhgc4
Cd276
Type_I_young
Type_II_young
Type_I_old
Type_II_old
B.
Hspb1
Gjb2
Mt1
Young
Old
10 μm
Young
Old
Mean Fluorescence Intensity
**
**
ns
Hspb1
Gjb2
Mt1

Figure 3: Vestibular HC aging is associated with the universal hallmarks. **A.** Complex heatmaps indicating the enrichment of genes associated with universal hallmarks of aging including senescence, loss of proteostasis, oxidative stress, autophagy, inflammaging, DNA damage repair, intercellular communication, and epigenetic alterations in the old vestibular HCs compared to young HCs. Single-cell counts were aggregated. Pseudo-bulk gene expression values were then scaled and log2-transformed. Expression values were centered by Cluster 3.0, and heatmaps were generated using JAVA TreeView. The color scale indicates the expression level. **B.** RNAscope *in situ* hybridization of *Hspb1* (proteostasis), *Gjb2* (intercellular communication) and *Mt1* (oxidative stress) in young and old vestibular sensory epithelia (n=2/age group). Mean fluorescence intensity was quantified and normalized to young group by ImageJ, and the p-values were calculated by unpaired t-test (**<0.01, ns - non-significant).

Figure 4

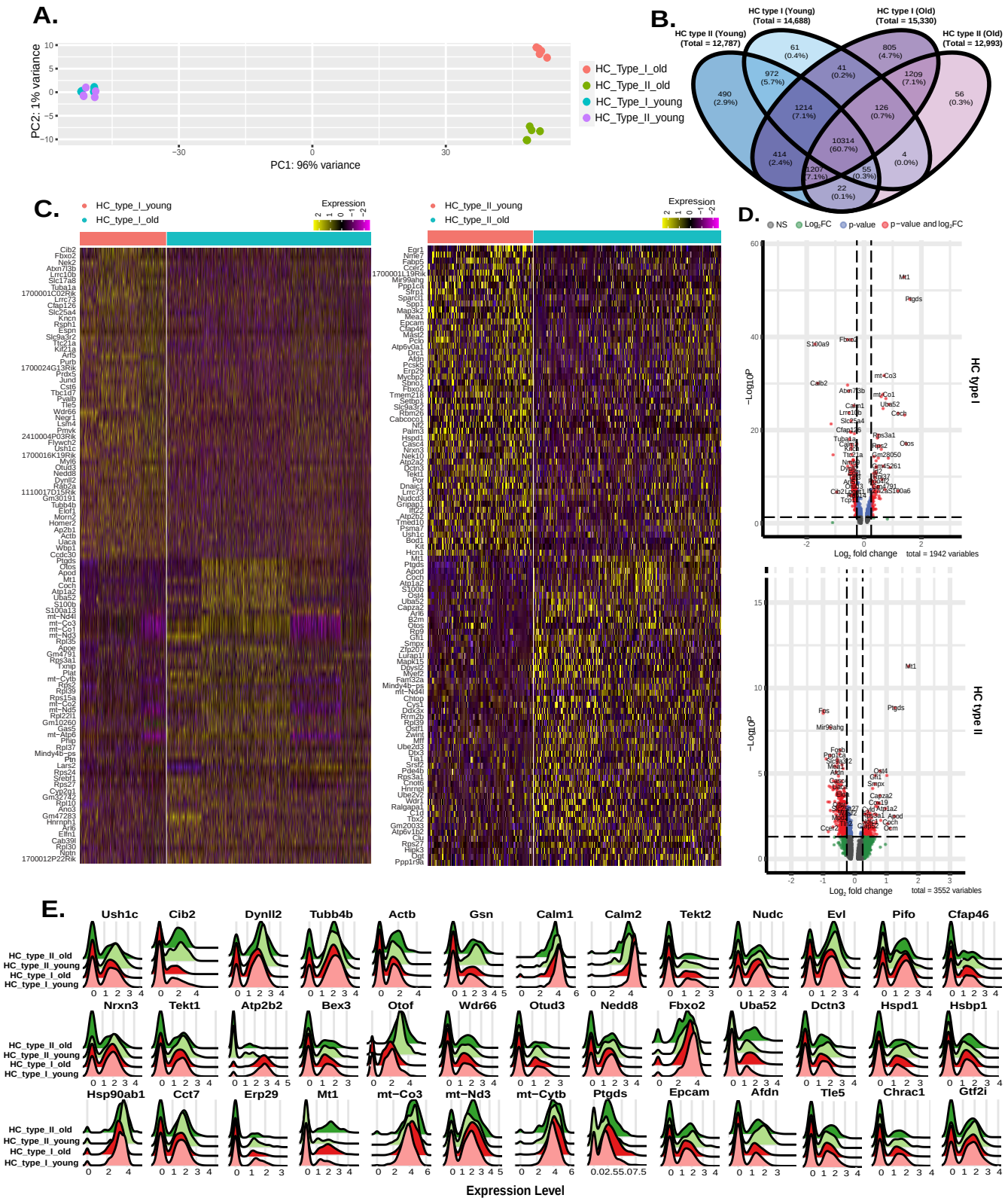
A.
PC2: 1% variance
PC1: 96% variance
HC_Type_I_old
HC_Type_II_old
HC_Type_I_young
HC_Type_II_young
B.
HC type I (Young) (Total = 14,688)
HC type I (Old) (Total = 15,330)
HC type II (Young) (Total = 12,787)
HC type II (Old) (Total = 12,993)
C.
HC_type_I_young
HC_type_I_old
HC_type_II_young
HC_type_II_old
Expression
D.
NS
Log2FC
p-value
p-value and log2FC
HC type I
HC type II
Log2 fold change
total = 1942 variables
total = 3552 variables
E.
Expression Level

Figure 4: Vestibular HC aging demonstrates cell type-specific aging signatures. **A.** Principle component (PC) multivariate analysis of young and old type I and II HC from the 5 biological replicates. DESeq2 in Seurat was used with the default Wald test, and multiple testing was corrected using the Benjamini-Hochberg method. Variance stabilizing transformation (VST) was applied to assess the variance among different conditions. **B.** Venn diagram indicating the number of shared and unique genes expressed in type I and II HCs indicating age-related transcriptomic changes. **C.** Heatmaps of young and old type I and II HCs indicating top 50 differentially expressed genes (DEGs). Rows represent genes, columns represent single cells, with expression levels ranging from high (purple) to low (yellow). $p<0.05$, FCcutoff - 0.25, logfc. threshold - 0.1). **D.** Volcano plots of young and old type I and II HCs demonstrating DEGs ($p<0.05$, FCcutoff - 0.25, logfc. threshold - 0.1). The x-axis represents the log2 fold-change values (avg_log2FC). The y-axis represents the raw p-values (p_val). Wilcoxon rank-sum test (with Bonferroni correction for false discovery FDR < 0.01) was used to analyze DEGs. **E.** Ridge plots of the genes associated with cell type-specific and universal hallmarks identified from DEG analysis. Gene expression distribution was estimated by Kernel density estimation (KDE).

Figure 5

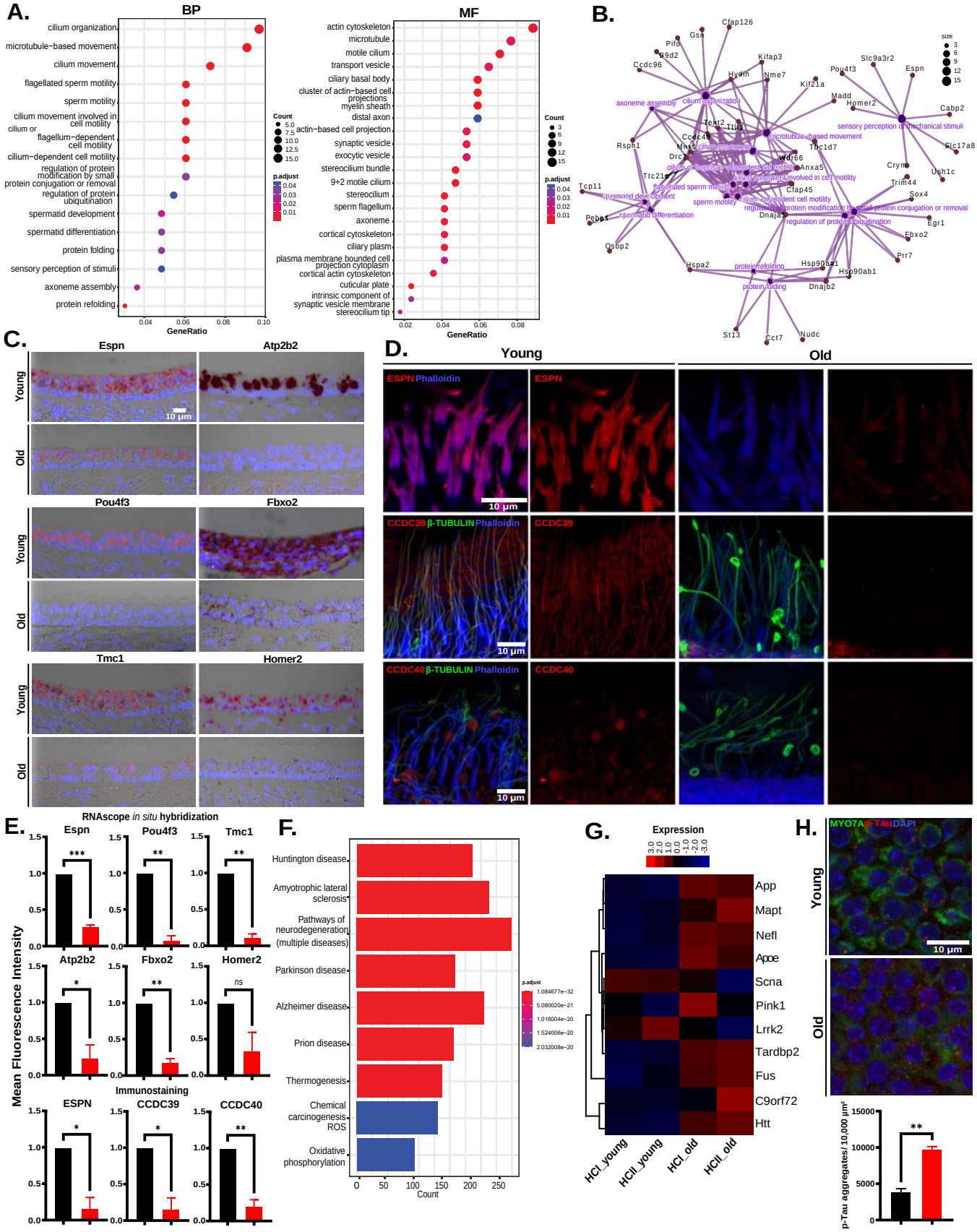

A.
BP
cilium organization
microtubule−based movement
cilium movement
flagellated sperm motility
sperm motility
cilium movement involved in cell motility
cilium or flagellum−dependent cell motility
cilium−dependent cell motility
regulation of protein modification by small protein conjugation or removal
regulation of protein ubiquitination
spermatid development
spermatid differentiation
protein folding
sensory perception of stimuli
axoneme assembly
protein refolding
GeneRatio
MF
actin cytoskeleton
microtubule
motile cilium
transport vesicle
ciliary basal body
cluster of actin−based cell projections
myelin sheath
distal axon
actin−based cell projection
synaptic vesicle
exocytic vesicle
stereocilium bundle
9+2 motile cilium
stereocilium
sperm flagellum
axoneme
cortical cytoskeleton
ciliary plasm
plasma membrane bounded cell projection cytoplasm
cortical actin cytoskeleton
cuticular plate
intrinsic component of synaptic vesicle membrane
stereocilium tip
Count
p.adjust
B.
size
C.
Espn
Atp2b2
Pou4f3
Fbxo2
Tmc1
Homer2
Young
Old
10 μm
D.
Young
Old
ESPN Phalloidin
ESPN
CCDC39 β-TUBULIN Phalloidin
CCDC39
CCDC40 β-TUBULIN Phalloidin
CCDC40
E.
RNAscope in situ hybridization
Mean Fluorescence Intensity
Immunostaining
ESPN
CCDC39
CCDC40
F.
Huntington disease
Amyotrophic lateral sclerosis
Pathways of neurodegeneration (multiple diseases)
Parkinson disease
Alzheimer disease
Prion disease
Thermogenesis
Chemical carcinogenesis ROS
Oxidative phosphorylation
Count
p.adjust
G.
Expression
App
Mapt
Nefl
Apoe
Scna
Pink1
Lrrk2
Tardbp2
Fus
C9orf72
Htt
HCI_young
HCII_young
HCI_old
HCII_old
H.
MYO7A p-Tau DAPI
Young
Old
10 μm
p-Tau aggregates/ 10,000 μm²

Figure 5: Biological processes downregulated in vestibular HCs with aging. **A.** Gene Ontology (GO) enrichment analysis of the biological process (BP) (left) and Molecular function (MF) (right). The Hypergeometric test with the Benjamini-Hochberg adjustment was used. Pairwise semantic similarity was computed for clustering the GO terms (p-value<0.05). **B.** Circular network (CNET) plot illustrating genes associated with the downregulated biological processes. **C.** RNAscope *in situ* hybridization validations of key HC genes identified from DEG and GO analysis (*Espn, Pou4f3, Tmc1, Atp2b2, Fbxo2, Homer2*) (n=2/age group). **D.** Immunostaining validations of age-related reduction in stereocilia-related (ESPN) and kinocilia-related (CCDC39, CCDC40) markers (red) (n=2/age group). **E.** Quantifications of RNAscope and immunostaining mean fluorescence intensity normalized to young group by ImageJ. P-values were calculated by unpaired t-test (*<0.05, **<0.01, ns - non-significant). **F.** Kyoto Encyclopedia of Genes and Genomes (KEGG) pathway analysis of old vestibular HC indicating enrichment of neurodegenerative diseases. The Hypergeometric test with the Benjamini-Hochberg p adjustment was used (p-value<0.05). **G.** Enrichment of Alzheimer's, Parkinson's, and Huntington's susceptibility genes in old vestibular HCs compared to young HCs. **H.** Immunostaining of p-Tau in young and old utricle wholemounts and quantification (n=2/age group).

Figure 6

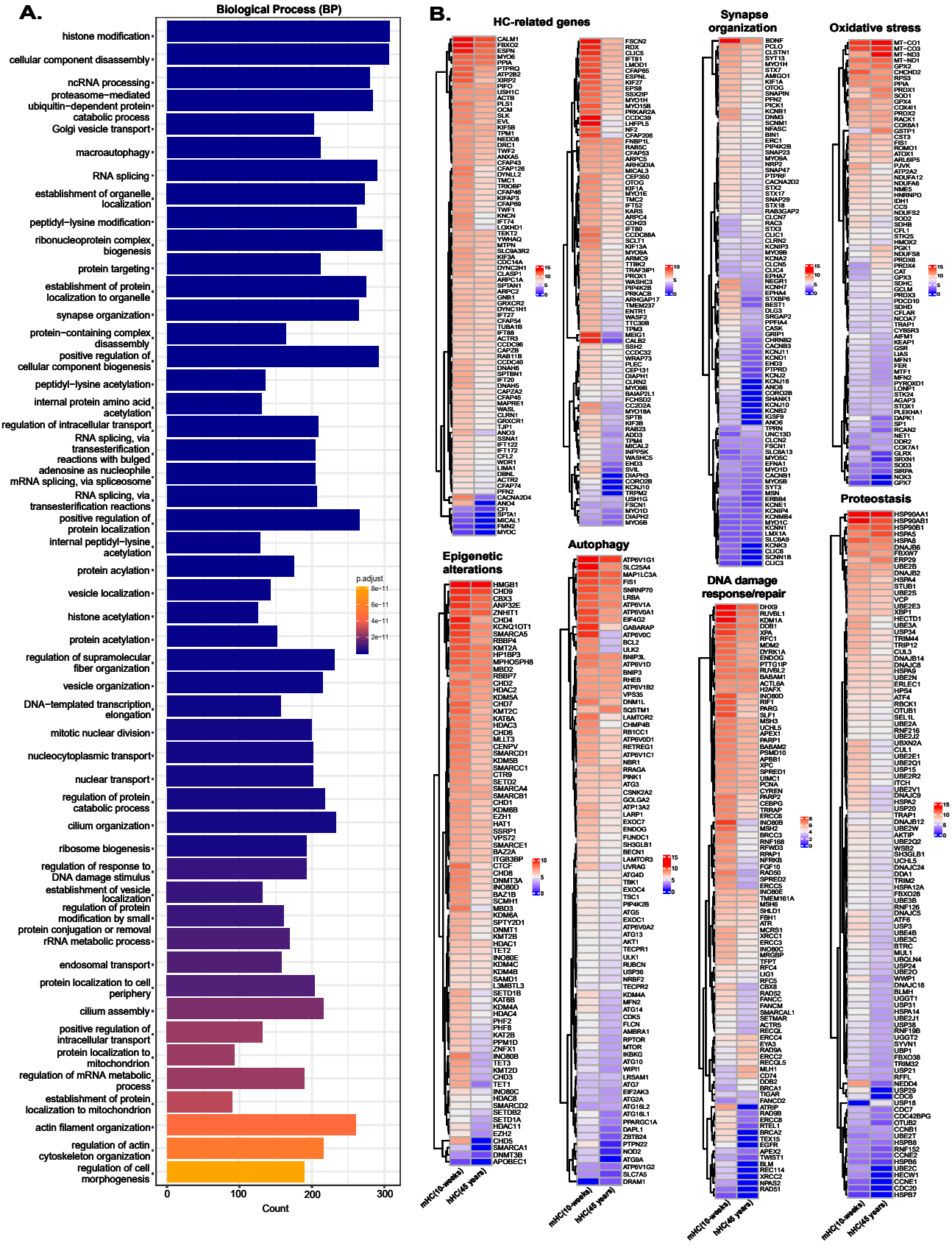
A.
Biological Process (BP)
histone modification
cellular component disassembly
ncRNA processing
proteasome−mediated ubiquitin−dependent protein catabolic process
Golgi vesicle transport
macroautophagy
RNA splicing
establishment of organelle localization
peptidyl−lysine modification
ribonucleoprotein complex biogenesis
protein targeting
establishment of protein localization to organelle
synapse organization
protein−containing complex disassembly
positive regulation of cellular component biogenesis
peptidyl−lysine acetylation
internal protein amino acid acetylation
regulation of intracellular transport
RNA splicing, via transesterification reactions with bulged adenosine as nucleophile
mRNA splicing, via spliceosome
RNA splicing, via transesterification reactions
positive regulation of protein localization
internal peptidyl−lysine acetylation
protein acylation
vesicle localization
histone acetylation
protein acetylation
regulation of supramolecular fiber organization
vesicle organization
DNA−templated transcription elongation
mitotic nuclear division
nucleocytoplasmic transport
nuclear transport
regulation of protein catabolic process
cilium organization
ribosome biogenesis
regulation of response to DNA damage stimulus
establishment of vesicle localization
regulation of protein modification by small protein conjugation or removal
rRNA metabolic process
endosomal transport
protein localization to cell periphery
cilium assembly
positive regulation of intracellular transport
protein localization to mitochondrion
regulation of mRNA metabolic process
establishment of protein localization to mitochondrion
actin filament organization
regulation of actin cytoskeleton organization
regulation of cell morphogenesis
p.adjust
8e−11
6e−11
4e−11
2e−11
0
100
200
300
Count
B.
HC-related genes
Synapse organization
Oxidative stress
Epigenetic alterations
Autophagy
DNA damage response/repair
Proteostasis
mHC(10-weeks)
hHC(45 years)

Figure 6: Universal and cell-type specific aging programs in human vestibular HCs. We aggregated scRNA-seq counts from our young (10-weeks) mice and publicly available human vestibular dataset (~45-year-old). Genes were mapped using ENSMBL IDs, and commonly expressed genes were combined to perform the downstream analysis as described in Methods. **A.** Gene Ontology (GO) enrichment analysis of top 50 downregulated biological processes in the human vestibular HCs. Hypergeometric test with the Benjamini-Hochberg p adjustment was used (p-value<0.05). **B.** Log2-transformed complex heatmaps of cell-type specific and universal aging signatures in the human vestibular HCs. The color scale represents the pseudobulk Log2-normalized expression values of the raw counts. Red to blue indicates high to low expression.

Figure 7

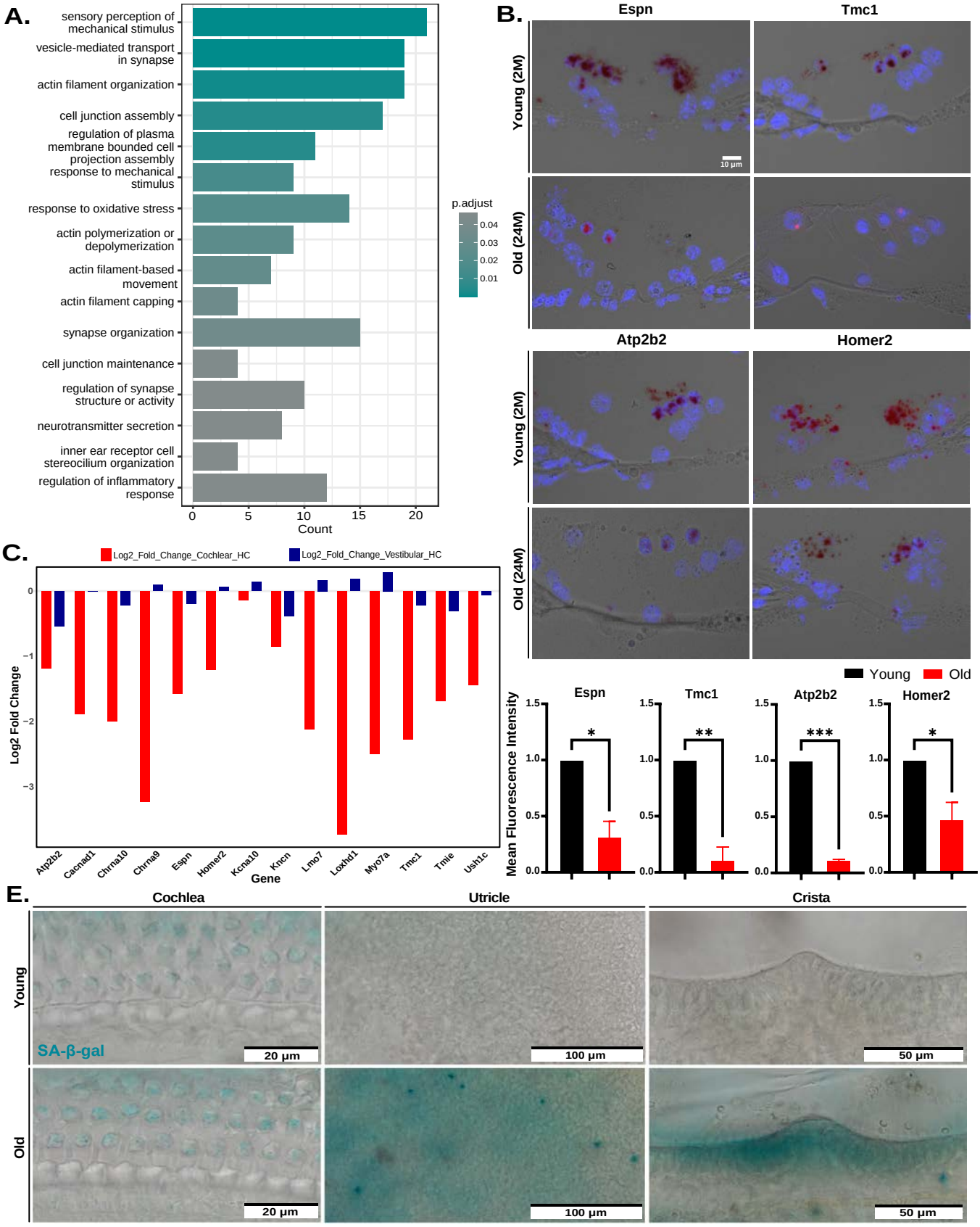
A.
sensory perception of mechanical stimulus
vesicle-mediated transport in synapse
actin filament organization
cell junction assembly
regulation of plasma membrane bounded cell projection assembly
response to mechanical stimulus
response to oxidative stress
actin polymerization or depolymerization
actin filament-based movement
actin filament capping
synapse organization
cell junction maintenance
regulation of synapse structure or activity
neurotransmitter secretion
inner ear receptor cell stereocilium organization
regulation of inflammatory response
0
5
10
15
20
Count
p.adjust
0.04
0.03
0.02
0.01
B.
Espn
Tmc1
Atp2b2
Homer2
Young (2M)
Old (24M)
10 μm
C.
Log2_Fold_Change_Cochlear_HC
Log2_Fold_Change_Vestibular_HC
Log2 Fold Change
0
−1
−2
−3
Atp2b2
Cacnad1
Chrna10
Chrna9
Espn
Homer2
Kcna10
Kncn
Lmo7
Loxhd1
Myo7a
Tmc1
Tmie
Ush1c
Gene
Young
Old
Mean Fluorescence Intensity
1.5
1.0
0.5
0.0
*
**
***
*
E.
Cochlea
Utricle
Crista
Young
Old
SA-β-gal
20 μm
100 μm
50 μm

Figure 7: Age-related alterations in cochlear HCs relative to vestibular HCs. **A.** Gene Ontology (GO) analysis showing biological processes downregulated in the old cochlear HCs compared to old vestibular HCs. The top genes that were downregulated in old cochlear HCs compared to age-matched old vestibular HCs were (Log2FC<0) used for this analysis using the Hypergeometric test with the Benjamini-Hochberg p adjustment ($p<0.05$). Pairwise semantic similarity was computed to cluster the GO terms. **B. and C.** RNAscope validations (B) and quantifications (C) showing age-related downregulation of HC function-related genes in old cochlear HCs compared to young cochlear HCs (n=2/age group). Mean fluorescence intensities were assessed and normalized to the young group by ImageJ, and p-values were calculated for each gene using unpaired t-test (*<0.05, **<0.01, ns-non-significant). **D.** Age-related Log2 fold changes of genes related to HC functions in cochlear and vestibular HCs. **E.** Senescence-associated β-galactosidase (SA-β-gal) activity in the cochlear and vestibular sensory epithelia with aging, indicating cellular senescence.

Supplementary information

Single-cell Transcriptomics Unravel Stereocilia Degeneration as a Key Contributor to Age-related Vestibular Dysfunction in Mice and Humans

Samadhi Kulasooriya[1*], Huizhan Liu[1], Sarath Vijayakumar[1], Celia Bloom[1], Su Tu[1], Ben J. Borgmeier[1], Mi Zhou[1], Litao Tao[1], Bechara Kachar[2], David Z. He[1*]

[1]Department of Biomedical Science, School of Medicine, Creighton University, Omaha, Nebraska, USA

[2]Laboratory of Cell Structure and Dynamics, National Institute of Deafness and Other Communication Disorders, National Institutes of Health, Bethesda, Maryland, USA

Corresponding authors:

David Z. He (DavidHe@creighton.edu)

Samadhi Kulasooriya (SamadhiKulasooriya@creighton.edu)

Supplementary Fig.1

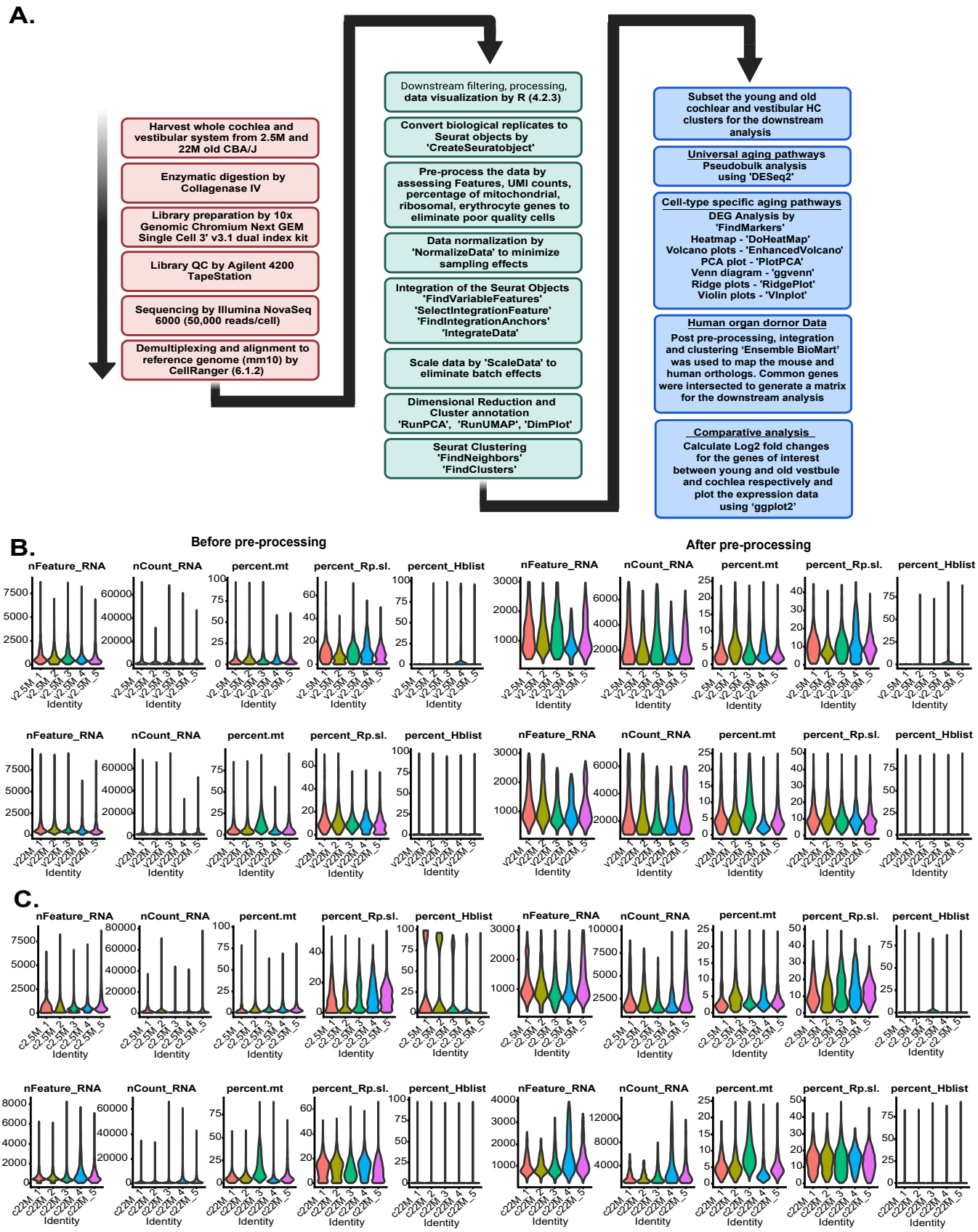

Supplementary Figure 1: Detailed scRNA-analysis workflow and pre-processing for quality control. **A.** The detailed computational workflow followed for the transcriptomic analysis. 2.5 and 22-month-old cochleae and vestibule were digested using collagenase IV, and sequencing libraries were prepared by 10x chromium next GEM single cell 3' v3.1, followed by QC assessment by Agilent 4200 TapeStation and sequencing by Illumina NoveSeq 6000 covering a depth of 50,000 reads/cell. Reads were demultiplexed and aligned by CellRanger. Downstream quality control and batch effect elimination were performed in R using Seurat and other packages. Once the clusters were annotated based on the known marker gene expression, HC clusters were subsetted from young and old samples to assess universal and cell-type specific aging signatures. Universal aging programs were evaluated via pseudobulk analysis, whereas cell-type specific aging programs were examined through DEG and GO/KEGG enrichment analysis. **B and C.** Violin plots depicting filtering parameters such as features, counts, mitochondrial, ribosomal, and erythrocyte gene percentages. B indicates data before filtering and C indicates after filtering in young (v2.5M), and old (v22M) vestibule, and young (c2.5M) and old (c22M) cochleae respectively.

Supplementary Fig.2

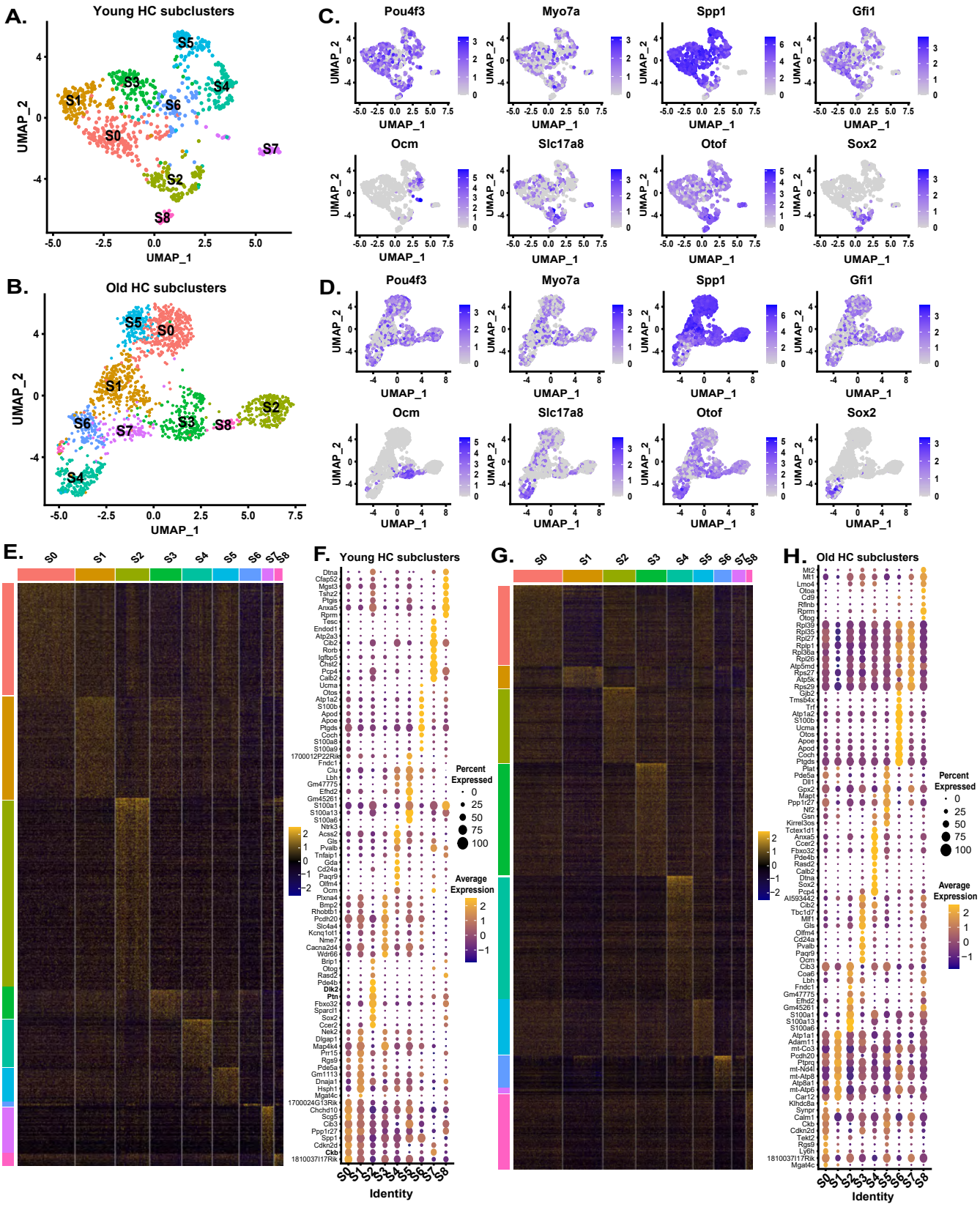

Supplementary Figure 2: Subclustering of young and old primary vestibular HC clusters reveals distinct HC subtypes. **A, B.** UMAPs indicate the presence of 9 transcriptionally distinct subclusters within the young and old primary HC clusters resolved at a cluster resolution of 1.5, respectively. **C, D.** Feature plots indicating the expression of type I and II HC-specific pan marker genes in the subclusters. **E, G.** Heatmaps demonstrating the top marker genes in each subcluster, indicating the transcriptional heterogeneity in the subclusters. **F, H.** Dot plots indicating the top 10 marker genes in each subcluster.

Supplementary Fig.3

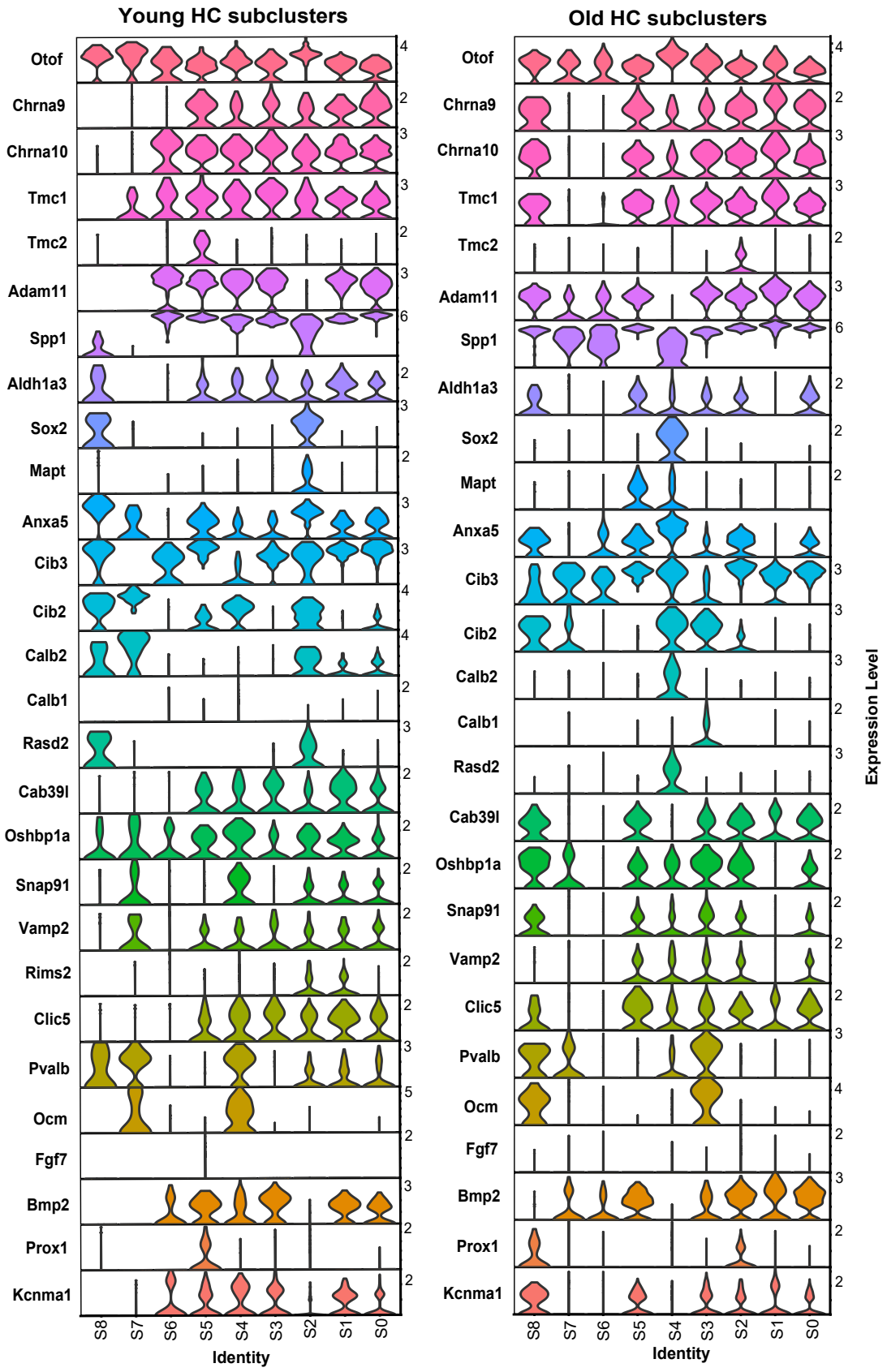

Supplementary Figure 3: Grid violin plots indicating the expression levels of the known marker genes of HC subtypes[38,80]. Type I HC markers: Spp1, Adam11, Tmc1, Chrna9, Chrna10, Type II HC markers: Sox2, Mapt, Anxa5, Slc17a8, Otof, striolar HC markers: Ocm, Pvalb, Tmc2, Cib2, Calb1, Kcnma1, extrastriolar HC markers: Rasd2, Osbpl1a, Cab39l, Rims2, Vamp2, Snap 91, Clic5, Cib3, Calb2, and crista HC markers: Prox1, Bmp2, Fgf7. According to the expression levels of these genes, young S0-S4, S6, and S7 can be categorized as extrastriolar type I HC clusters, S2 and S8 as extrastriolar type II clusters, and S5 as a Crista type I HC cluster. For the old subclusters, S0, S1, and S5 can be classified as extrastriolar type I HC, S4 as extrasriolar type II HC, S3 and S7 as striolar type I HC, and S2 as crista HC.

Supplementary Fig.4

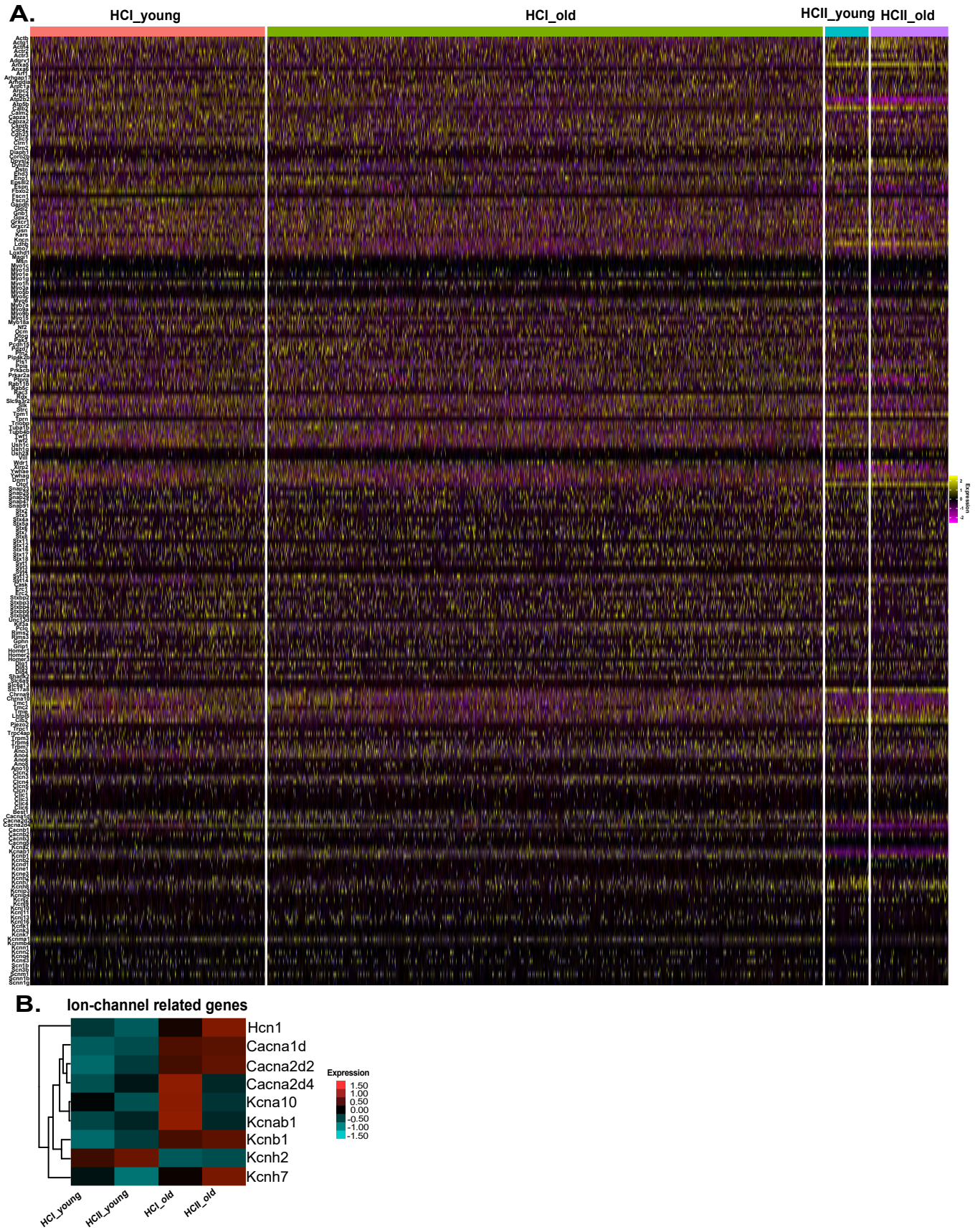

Supplementary Figure 4: A. HC-related gene (stereocilia, synapse and ion channel) expression in type I and II HCs at the individual cell level indicating heterogeneity. **B.** Age-related changes in the key ion-channel related genes in vestibular HCs.

Supplementary Fig.5

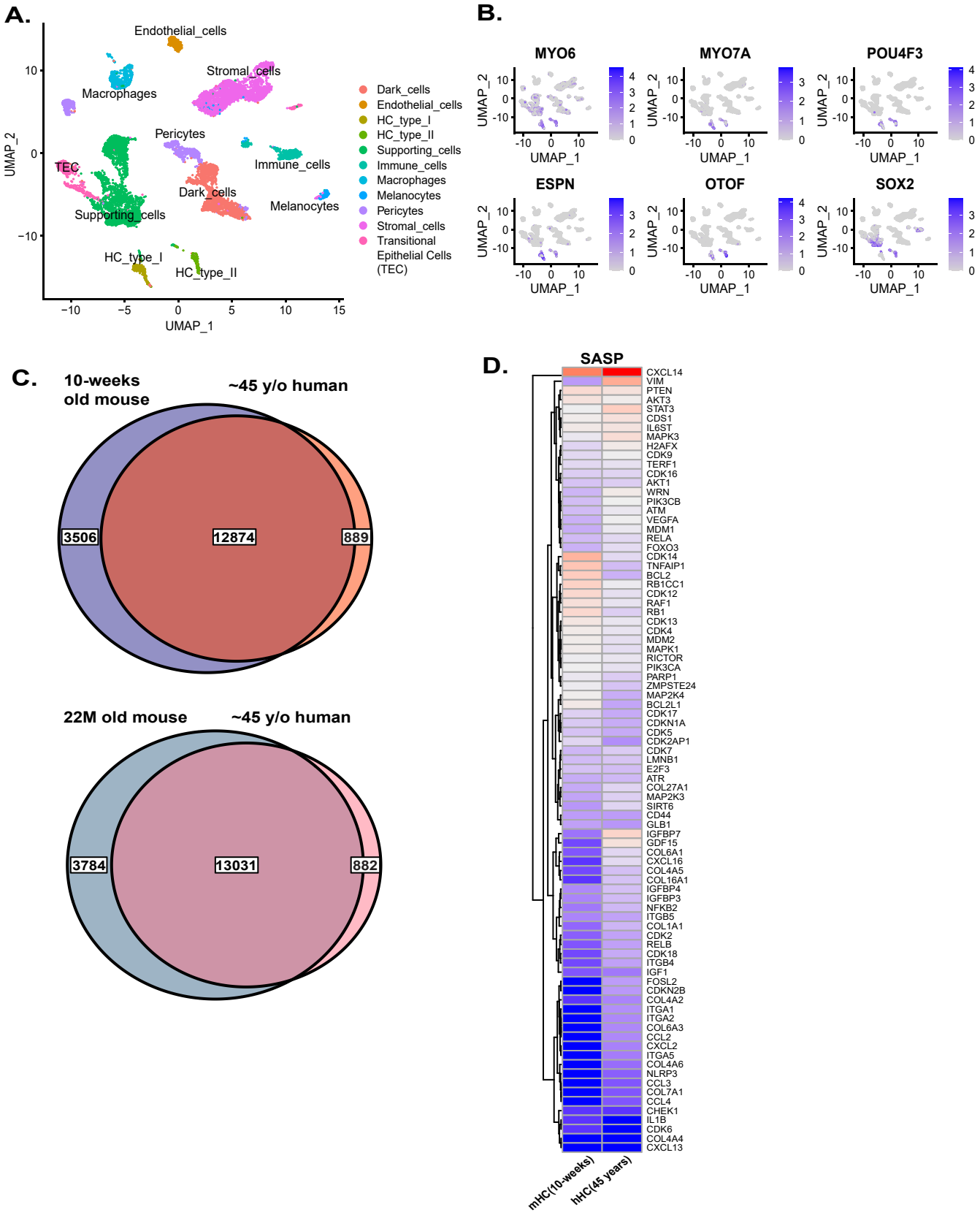

Supplementary Figure 5: Cell-type distribution and gene mapping of murine and human organ donor transcriptomes**. A.** UMAP plot showing the distribution of cell types in human vestibular samples. **B.** Feature plot indicating vestibular HC clusters based on known marker gene expression. **C.** Venn diagrams depicting the number of distinct and overlapping genes between murine (2.5 and 22 months) and human data sets, respectively. **D.** SASP associated gene expression in human vestibular HCs.

Supplementary Fig.6

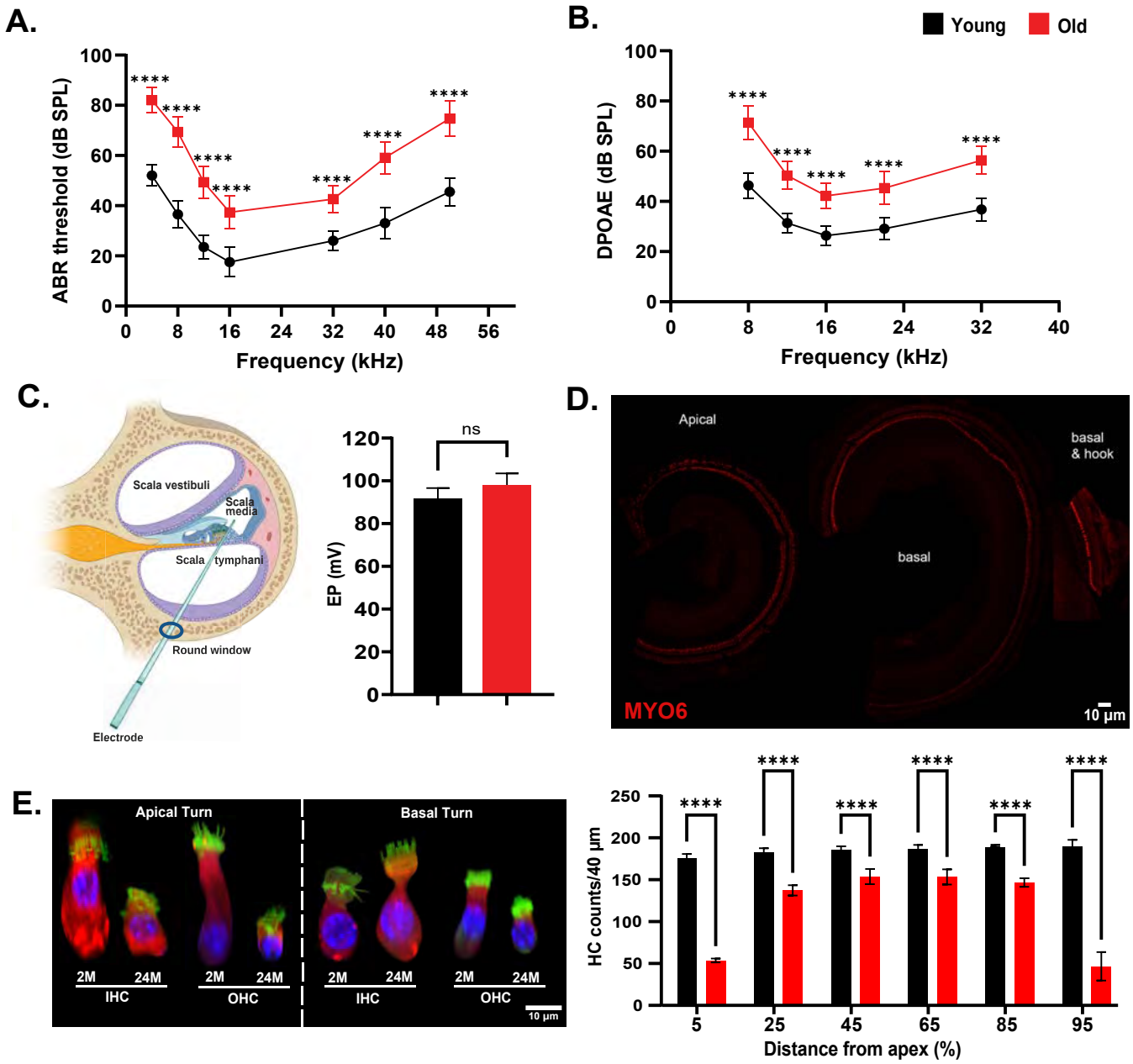

Supplementary Fig. 6: Age-related auditory functional and morphological changes. **A-C.** Auditory brainstem response (ABR), distortion product otoacoustic emissions (DPOAE), and endocochlear potential (EP) in young (n = 8/per age group) CBA/J (*P<0.05, ** P<0.01, ***P<0.001, ****P<0.0001, ns - non-significant). **D.** Representative images of the cochlea immunolabeled with anti-MYO6 and the HC quantification along the tonotopic organization. **E.** Confocal virtual sectioning images of individual HC morphology demonstrating cellular hypertrophy and atrophy in IHC and OHCs from apical and basal turns with aging. Virtual sections were imaged using Imaris, and the background was removed using Adobe Photoshop.

Supplementary Fig.7

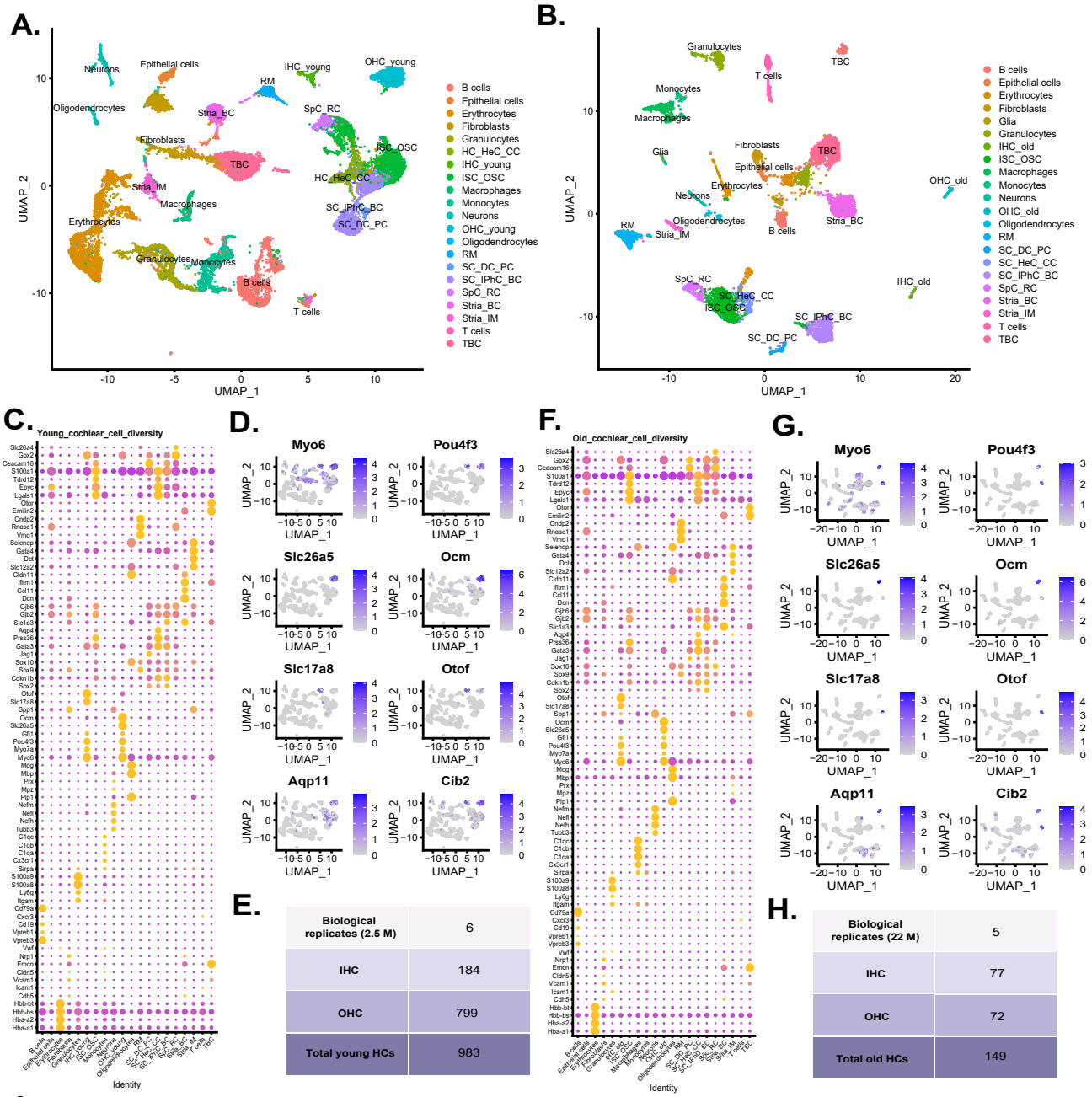

Supplementary Fig. 7: Young (2.5M) and old (22M) cochlear cell type distribution. **A, B.** Uniform manifold approximation and projection (UMAP) plot shows the distribution of different cell types in young and old cochlear samples. **C, F.** Dot plots indicating the expression of known marker genes used to identify the cell types and subsequent cluster annotation shown in B and C. The dot size represents the percentage of cells expressing the genes from each cluster, whereas the color indicates the expression level. Expression levels are normalized via z-score normalization. Thus, the average expression is zero, and positive or negative values indicate expression above or below average. **D, G.** Feature plots demonstrating the HC-specific pan marker gene expression in the HC clusters identified in the UMAPs. **E, H.** Number of inner and outer HCs identified from young and old cochlear samples for the downstream analysis. 7-8 mice were used per biological replicate, and a total of 5 biological replicates were used for the transcriptomic analysis. **I.** Downregulated GO terms related to universal processes in old cochlear HCs compared to old vestibular HCs.